Title
Triple-quantum Filtered NMR Imaging of Sodium in the Human Brain

Author
Keltner, J.R.

Publication Date
1993-04-30

LBL-34375
UC-408

Lawrence Berkeley Laboratory
UNIVERSITY OF CALIFORNIA

Triple-Quantum Filtered NMR Imaging of Sodium in the Human Brain

J.R. Keltner
(Ph.D. Thesis)

April 1993

Donner Laboratory

Biology & Medicine Division

Prepared for the U.S. Department of Energy under Contract Number DE-AC03-76SF00098

DISCLAIMER

LBL-34375

Triple-Quantum Filtered NMR Imaging of Sodium in the Human Brain

John Robinson Keltner
Ph.D. Thesis

Department of Physics
University of California at Berkeley

and

Lawrence Berkeley Laboratory
University of California
Berkeley, CA 94720

April 1993

This work was supported by the National Institutes of Health under Grant HL 25840 and Grant HL 07367, through the U.S. Department of Energy under Contract No. DE-AC03-76SF00098 and by the National Science Foundation under Grant 89-20133

Abstract

Triple-Quantum Filtered NMR Imaging of Sodium-23 in the Human Brain

by

John Robinson Keltner

Doctor of Philosophy

University of California at Berkeley

Professor Erwin L. Hahn, Chair

In the past multiple-quantum filtered imaging of biexponential relaxation sodium-23 nuclei in the human brain has been limited by low signal to noise ratios; this thesis demonstrates that such imaging is feasible when using a modified gradient-selected triple-quantum filter at a repetition time which maximizes the signal to noise ratio. Nuclear magnetic resonance imaging of biexponential relaxation sodium-23 (^{23}Na) nuclei in the human brain may be useful for detecting ischemia, cancer, and pathophysiology related to manic-depression. Conventional single-quantum NMR imaging of *in vivo* biexponential relaxation ^{23}Na signals is complicated by the presence of single-exponential relaxation ^{23}Na signals. Multiple-quantum filters may be used to selectively image biexponential relaxation ^{23}Na signals since these filters suppress single-exponential relaxation ^{23}Na signals.

In this thesis, the typical repetition times (200 - 300 ms) used for *in vivo* multiple-quantum filtered ^{23}Na experiments are shown to be approximately 5 times greater than the optimal repetition time which maximizes multiple-quantum filtered SNR. Calculations and experimental verification show that the gradient-selected triple-quantum (GS3Q) filtered SNR for ^{23}Na in a 4% agarose gel increases by a factor of two as the repetition time decreases from 300 ms to 55 ms. The measured relaxation times of the ^{23}Na in the 4% agarose gel were similar to *in vivo* ^{23}Na relaxation times.

It is observed that a simple reduction of repetition time also increases spurious single-quantum signals from GS3Q filtered experiments. Irreducible superoperator calculations have been used to design a modified GS3Q filter which more effectively

suppresses the spurious single-quantum signals. The modified GS3Q filter includes a preparatory crusher gradient and two-step-phase cycling. The suppression of spurious single-quantum signals by the modified GS3Q filter is calculated and experimentally verified.

Using the modified GS3Q filter and a repetition time of 70 ms, a three dimensional triple-quantum filtered image of a phantom modelling ^{23}Na in the brain was obtained. The phantom consisted of two 4 cm diameter spheres inside of a 8.5 cm x 7 cm ellipsoid. The two spheres contained 0.012 and 0.024 M ^{23}Na in 4% agarose gel. Surrounding the spheres and inside the ellipsoid was 0.03 M aqueous ^{23}Na. The image dimensions were 16 x 16 x 16 voxels with the dimension of a voxel being 1.5 x 1.5 x 1.5 cm^3. The signal to noise ratio for the GS3Q filtered ^{23}Na signal from the 0.012 and 0.024 M ^{23}Na spheres was 17 and 30 for a 54 minute experiment at 2.35 T. These imaging results indicate that it should be possible to obtain a modified GS3Q filtered image of 0.012 M biexponential relaxation ^{23}Na in the human brain in 30 minutes with a voxel size of 2 x 2 x 2 cm^3 and a SNR of 10 at 2.35 T.

E. L. Hahn

.....

Prof. E. L. Hahn, Chair

Acknowledgments

My sincerest gratitude goes to my thesis committee member Professor Thomas Budinger, Dr. Mark Roos, and Dr. Sam Wong. Their generous guidance, support and unending patience have guided me to this milestone. It is with great enthusiasm that I look forward to working with them in the future. I wish to thank my thesis committee member, Professor Erwin Hahn, for his persistence in making sure that I learned my physics. My year working with his students David Newitt and Larry Wald was very special. I would also like to thank my third thesis committee member, Professor Carson Jeffries. I am indebted to my dear friends at the Center for Functional Imaging: Blaise Frederick, Josh Lack, Paul Hughett, Dr. Bill Moses and especially Dr. Winston Sun for his warmth and teaching me how to play golf.

My friendships with Jeff Walker, Raj Vaswani, George Keisidis, Corbet Wilcox, Mimi Wang, and Tim Wong have been very important to me. I will miss rooming with Jeff, late night brooding with Raj, George's insanity, Corbet's patience as well as Mimi's and Tim's smiles.

I am indebted to my family. My heart will always be with my globe-trotting brothers Carter and Brent. I offer my deepest thanks to my parents John and Nancy who gave me life. Your love and encouragement are my foundation.

Finally, I give my love to Jill. It is hard to find the words to thank you. You have held me when I cried. You have glowed when I have succeeded. I am yours.

This work was supported by the National Institutes of Health under Grant HL 25840 and Grant HL 07367, and by the National Science Foundation under Grant 89-20133, through the U.S. Department of Energy under Contract No. DE-AC03-76SF00098.

Contents

GLOSSARY

1Q Single-Quantum

2Q Double-Quantum

3Q Triple-Quantum

BER Biexponential Relaxation

EFG Electric Field Gradient

FID Free Induction Decay

GSMQ Gradient-Selected Multiple-Quantum Coherence

M1QC Single-Quantum Coherence from Multiple-Quantum Coherence

MQ Multiple-Quantum

MQC Multiple-Quantum Coherence

NMR Nuclear Magnetic Resonance

O1QC Single-Quantum Coherence from Other than Multiple-Quantum Coherence

PCMQ Phase-Cycled Multiple-Quantum Coherence

SEFG Static Electric Field Gradient

SER Single-Exponential Relaxation

SNR Signal to Noise Ratio

SNR_{3Q} Signal to Noise Ratio of Triple-Quantum Coherence

Chapter 1

Introduction

1.1 Statement of Thesis

The purpose of this thesis is to determine the feasibility of multiple-quantum filtered nuclear magnetic resonance imaging of biexponential relaxation sodium-23 signals from the human brain. Biexponential relaxation (BER) sodium-23 (^{23}Na) NMR signals have been used to detect ischemia and cancer and may be useful for detecting pathophysiology associated with manic-depression [1, 2, 3]. BER ^{23}Na signals result from quadrupole interactions between the nuclei of ^{23}Na ions and electric field gradients from biological macromolecules [4]. Asymmetries in biexponential relaxation result in BER ^{23}Na nuclei producing multiple-quantum (MQ) coherences. Interactions between the nuclei of ^{23}Na ions and electric field gradients from water molecules produce single-exponential relaxation (SER) ^{23}Na signals [4]. The symmetry of single-exponential relaxation results in SER ^{23}Na nuclei only producing single-quantum (1Q) coherences. Detecting BER ^{23}Na 1Q signals is complicated by the presence of SER ^{23}Na signals. Multiple-quantum filters may be used to selectively detect BER ^{23}Na signals since these filters suppress SER ^{23}Na signals [5].

MQ filtered imaging has been used to image BER ^{23}Na NMR signals [2, 6, 7, 8, 9, 10]. However, until now MQ NMR imaging of BER ^{23}Na signals from the human brain has required prohibitively long imaging times due to low signal to noise ratios

(SNR). This thesis demonstrates that repetition times presently used for MQ NMR imaging of *in vivo* BER ^{23}Na signals are approximately five times larger than the optimal repetition time which maximizes the MQ filtered SNR. It also demonstrates that conventional MQ filters fail to suppress unwanted spurious 1Q signals for short repetition times. Consequently, in this thesis a modified gradient-selected triple-quantum (GS3Q) filter is developed which yields improved suppression of spurious 1Q signals at short repetition times. Experiments and calculations are performed to characterize the performance of this modified GS3Q filter. Using the modified GS3Q filter with short repetition times, GS3Q images of a phantom with physiological concentrations of ^{23}Na are obtained. By performing this GS3Q filtered imaging of a phantom, it is determined that the modified GS3Q filter imaging technique presented here may be successfully used for imaging BER ^{23}Na in the human brain.

1.2 Physiology of Sodium Ions

The major role of sodium ions in biological systems is maintenance of membrane potentials along with other ions such as potassium. Active transport of ^{23}Na out of the cell produces an intracellular ^{23}Na concentration of 15 mM and the extracellular ^{23}Na concentration of 150 mM. In addition to maintaining the membrane potential, the large difference in ^{23}Na concentration is used also as a free energy reserve for the control of a number of critical cellular functions: size, pH, glucose concentration, growth, and proliferation [11].

The essential role of ^{23}Na in the cell makes it suspect of being involved in the mechanisms of ischemia, cancer, and manic-depression. Ischemia, lack of blood flow, leading to lack of oxygen has been shown to produce 4 mM increases in the intracellular ^{23}Na concentration of cells [12]. Lack of oxygen in a cell forces it to produce lactic acid which decreases the intracellular pH. The primary mechanism for raising the cellular pH is to exchange intracellular protons for extracellular ^{23}Na [13]. It has been observed that the intracellular ^{23}Na concentration increases in cancer cells [14].

The biophysical mechanism for this increase is not clear [11]. In a recent review of research on manic-depression, it is concluded that dysfunction of membrane proteins utilizing or maintaining ^{23}Na concentration imbalances are likely to be part of the mechanism(s) giving rise to manic-depression [15].

1.3 Physical Environment of Sodium Ions

The dominant mechanism for the relaxation of the ^{23}Na NMR signal is the coupling of the ^{23}Na nuclear quadrupole moment with fluctuating electric field gradients (EFGs). For a spin-3/2 nucleus, quadrupolar relaxation gives rise to biexponential relaxation when the EFGs fluctuate at approximately the same rate as the spin's Larmor frequency. At 2.35 Tesla the ^{23}Na Larmor frequency is approximately 10^8 Hz. Sodium nuclei experience EFGs fluctuating at approximately 10^8 Hz when they interact with large biological molecules. Agarose gels contain large polysaccharide molecules. Agarose gels containing ^{23}Na ions are used in this thesis as a model system for BER ^{23}Na ions in biological systems. The relaxation times for ^{23}Na ions in agarose gels are similar to the relaxation times of *in vivo* BER ^{23}Na signals [16, 3, 17]. If the electric field gradients fluctuate much faster than the ^{23}Na Larmor frequency, then the ^{23}Na undergoes single-exponential relaxation. The EFGs from water molecules forming a hydration shell around ^{23}Na ions fluctuate at approximately 10^{12} Hz and produce SER ^{23}Na signals.

The BER ^{23}Na signal has been shown to be produced by both the intracellular and extracellular ^{23}Na [18, 19, 20]. The BER signals are probably not useful for quantitatively measuring intracellular ^{23}Na. It has been suggested, however, that the BER ^{23}Na signals may be useful for detecting increases in intracellular ^{23}Na ions [3]. A number of experiments have been performed in which increased BER ^{23}Na signals were detected in the presence of ischemia [3, 21, 22]. The increases in the BER ^{23}Na signals are thought to result from ^{23}Na influxes into the intracellular space. In another application, it has been shown that the BER ^{23}Na signals from tumors are increased

[14]. It is thought that increased intracellular ^{23}Na ion concentration in these tumors may be responsible for the increased amount of BER ^{23}Na signal they produce. A contribution of this thesis it to suggest that BER ^{23}Na signals may also be useful for studying manic-depression.

1.4 Detecting BER Sodium Signals

A number of approaches have been proposed for measuring *in vivo* BER ^{23}Na signal amplitudes. One method is to subtract an image obtained from an initial free induction decay and an image obtained from a subsequent echo [14]. Another method is to fit the acquired free induction decay to a sum of exponentials [23, 24]. A third method is to use an inverse Laplace Transform to estimate a distribution of relaxation times [25, 26]. The most significant drawback of using these approaches is that the *in vivo* BER ^{23}Na signal is difficult to measure accurately since it is much smaller than the *in vivo* SER ^{23}Na signal.

It has been shown that multiple-quantum filtering techniques [27] can be used to suppress the dominant SER signal and only detect the BER ^{23}Na [5]. This approach utilizes the fact that the BER ^{23}Na produces MQ signals in addition to normal 1Q signals. In Chapter 2, it is shown that asymmetries in biexponential relaxation result in BER ^{23}Na nuclei producing MQ coherences. The symmetry of single-exponential relaxation results in SER ^{23}Na nuclei not producing multiple-quantum coherences. The MQ signals are easily separated from the 1Q signals by using the increased rate of precession of MQ signals. This approach allows much more accurate measurement of the amount of BER ^{23}Na than do the previous approaches.

The drawback of the MQ approach is that the MQ signals are weaker than the 1Q signals. The low SNR of the *in vivo* ^{23}Na MQ signals requires prohibitively long imaging times for *in vivo* imaging experiments. However, in a fixed time one can improve the NMR SNR by decreasing the repetition time of the NMR experiment so more signals are collected and by averaging the signals [28]. This approach to

improving the signal to noise is only limited by the repetition time of the experiment becoming so short that the nuclear spins saturate. To calculate the optimum repetition time which balances averaging and saturation it is necessary to perform a detailed analyses of the nuclear spins evolution during repeated pulses. This analysis is complicated for ^{23}Na by the four energy levels for a spin-3/2 nuclei and six different relaxation times. In this thesis an exact description of sodium's evolution during repeated RF hard pulses is used to show that the GS3Q SNR improves by a factor of two when using an optimum repetition time instead of typical repetition times for GS3Q filtered experiments with ^{23}Na in an agarose gel. This improved SNR leads to reductions of the imaging time by a factor of four. These calculations were verified using GS3Q filtered experiments with ^{23}Na in an agarose gel.

The use of short repetition times with MQ filters has not been previously successful because conventional MQ filters fail to suppress the unwanted 1Q signal. It is critical to the performance of conventional MQ filters that they act upon nuclear spins in thermal equilibrium. Such nuclear spins have their magnetization aligned along the axis defined by the static magnetic field, typically the Z-axis. Conventional MQ filters are not able to suppress magnetization transverse to the static magnetic field. Therefore, conventional MQ filters fail at short repetition times since not all of the transverse magnetization relaxes to thermal equilibrium during the short inter-filter interval.

In this thesis an improved GS3Q filter is developed which suppresses the 1Q signal at short repetition times better than conventional GS3Q filters. The improved GS3Q filter functions at short repetition times by dephasing residual transverse magnetization with a preparatory crusher gradient. A phase cycling sequence of limited length is also used to help minimize the amount of spurious 1Q signals by subtracting them while adding the 3Q signals. Long phase cycling sequences may not be used in imaging experiments since the imaging time becomes too long.

1.5 MQ Filtered Imaging

A number of groups have imaged MQ ^{23}Na signals [2, 6, 7, 8, 9, 10]. This thesis expands upon these efforts by using the modified GS3Q filter to determine what spatial resolution is obtainable for GS3Q filtered images of BER ^{23}Na in the human brain. A three dimensional image of a phantom consisting of a 8.5 cm long ellipsoid containing two 4 cm diameter spheres is obtained using the improved GS3Q filter. In between the spheres and ellipsoid was 0.030 M NaCl and inside the spheres were 0.012 and 0.024 M NaCl in 4 percent agarose gels. The three dimensional GS3Q filtered ^{23}Na image of the phantom demonstrates that 3D GS3Q filtered ^{23}Na imaging of the human brain is feasible. Using the techniques presented in this thesis with a conventional quadrature head probe, a repetition time of 70 ms and a voxel size of 2 x 2 x 2 cm^3, it should be possible to image GS3Q filtered 0.012 M BER ^{23}Na signals in 30 minutes with a SNR of 10 at 2.35 T.

Chapter 2

Theory Of MQ Filtering

This chapter reviews the theoretical issues upon which this thesis is based. Particular emphasis is placed upon examining why the anti-phase coherence state is the transition state between single-quantum and multiple-quantum coherences. In Section 2.1, the creation of multiple-quantum coherence by quadurpole interactions with static electric field gradients is discussed. In Section 2.2, the creation of multiple-quantum coherence by quadrupole interactions with fluctuating electric field gradients is discussed. In Section 2.3, approaches for detecting multiple-quantum coherences are reviewed and a modified gradient-selected triple-quantum filter is presented.

2.1 Multiple Quantum Coherences

Multiple quantum coherences are discussed in a number of references [29, 30] and review articles [31, 32, 33]. In this discussion of multiple quantum coherences (MQCs) an intuitive explanation of why the anti-phase coherence state is the transition spin state between single quantum coherence and multiple quantum coherence is attempted. The explanation proceeds by examining the dynamics of an isolated spin-3/2 system and a quadrupole split spin-3/2 system.

The thermal equilibrium population distribution of a isolated spin-3/2 spin system in a static magnetic field H_o aligned along the Z-axis, may be described with the density operator [29],

$$\rho = \frac{\hbar\gamma H_o}{kT} I_z, \tag{2.1}$$

where the spin dipole moment is $\vec{\mu} = \hbar\gamma\vec{I}$ and it is assumed that $\hbar\gamma H_o << kT$. In terms of the spin-3/2 energy eigenfunctions, the matrix representation of the equilibrium density operator is

$$\rho = \frac{\hbar\gamma H_o}{kT} \begin{pmatrix} -\frac{3}{2} & 0 & 0 & 0 \\ 0 & -\frac{1}{2} & 0 & 0 \\ 0 & 0 & \frac{1}{2} & 0 \\ 0 & 0 & 0 & \frac{3}{2} \end{pmatrix}. \tag{2.2}$$

The diagonal elements of the matrix are the magnetic quantum numbers for the four energy eigenstates. Combined with the coefficients in front of the density matrix the diagonal terms represent the population of the energy states. It is important that in the high temperature limit, $\hbar\gamma H_o << kT$, the population decreases of the upper two energy levels balance the population increases of the lower two energy levels. The population differences among the four energy levels produces net magnetization parallel to the H_o field which may be described with the Curie Law [34],

$$M_z = \hbar\gamma Tr < I_z\rho >= \frac{(\hbar\gamma)^2 \frac{3}{2}(\frac{3}{2}+1)}{3kT} \tag{2.3}$$

The equation of motion for the density operator is

$$\frac{d\rho}{dt} = \frac{i}{\hbar}[\rho, H], \tag{2.4}$$

where H is the Hamiltonian. The solution to this equation is the evolution equation,

$$\rho(t) = e^{-\frac{i}{\hbar}Ht}\rho(0)e^{\frac{i}{\hbar}Ht}. \tag{2.5}$$

When an appropriate duration radiofrequency (RF) magnetic field B_y is applied

to the nuclear spins, the equilibrium magnetization aligned along the Z-axis rotates down to the X-axis [35, 36]. This rotation may be described using the evolution equation for the density operator,

$$e^{-i\frac{\pi}{2}I_y}\left(\frac{\hbar\gamma H_o}{kT}I_z\right)e^{i\frac{\pi}{2}I_y} \xrightarrow{90^y} \frac{\hbar\gamma H_o}{kT}I_x. \tag{2.6}$$

The matrix representation of the density operator describing the transverse magnetization is

$$\rho = \frac{\hbar\gamma H_o}{kT}\begin{pmatrix} 0 & \frac{\sqrt{3}}{2} & 0 & 0 \\ \frac{\sqrt{3}}{2} & 0 & 1 & 0 \\ 0 & 1 & 0 & \frac{\sqrt{3}}{2} \\ 0 & 0 & \frac{\sqrt{3}}{2} & 0 \end{pmatrix}. \tag{2.7}$$

The off-diagonal density matrix elements describe coherent superposition states [29] between adjacent energy eigenstates. These coherent superposition states are referred to as single quantum coherence (1QC). Examination of the transverse density matrix reveals that there are three separate 1QCs. The transverse magnetization is obtained from the density operator using

$$M_x = \hbar\gamma Tr < I_x\rho > . \tag{2.8}$$

Interactions between the nuclear spins and their surrounding environment produce dephasing of the 1QCs. This irreversible dephasing is called T_2 relaxation. In this example it is assumed that the T_2 relaxation for the three 1QCs may be described by the same exponential decay e^{-t/T_2}. After a relaxation period of t, the density matrix becomes

$$\rho = e^{-t/T_2}\frac{\hbar\gamma H_o}{kT}\begin{pmatrix} 0 & \frac{\sqrt{3}}{2} & 0 & 0 \\ \frac{\sqrt{3}}{2} & 0 & 1 & 0 \\ 0 & 1 & 0 & \frac{\sqrt{3}}{2} \\ 0 & 0 & \frac{\sqrt{3}}{2} & 0 \end{pmatrix}. \tag{2.9}$$

We are ignoring relaxation among the nuclear spin populations (T_1 relaxation). Applying a 2nd 90° pulse, the transverse magnetization is rotated into inverted Z-magnetization,

$$\rho = e^{-t/T_2}\frac{\hbar\gamma H_o}{kT}\begin{pmatrix} \frac{3}{2} & 0 & 0 & 0 \\ 0 & \frac{1}{2} & 0 & 0 \\ 0 & 0 & -\frac{1}{2} & 0 \\ 0 & 0 & 0 & -\frac{3}{2} \end{pmatrix}. \tag{2.10}$$

The isolated spin system yields remarkably balanced behavior. The first RF pulse rotated the system into only three 1QCs. The second RF pulse rotated the three 1QCs completely into an inverted population state. The balanced dynamics of the isolated spin system are the result of the high temperature Boltzman distribution of the initial state and the single T_2 relaxation rate. Consider the dynamics of a unbalanced spin system whose spins are only in the lowest energy state. A single RF rotation on this system yields a more complicated density matrix,

$$\frac{\hbar\gamma H_o}{kT}\begin{pmatrix} 0 & 0 & 0 & 0 \\ 0 & 0 & 0 & 0 \\ 0 & 0 & 0 & 0 \\ 0 & 0 & 0 & \frac{1}{2} \end{pmatrix} \xrightarrow{90^y} \frac{\hbar\gamma H_o}{kT}\begin{pmatrix} 0.1 & -i0.1 & -0.1 & i0.06 \\ i0.1 & 0.2 & 0-i.2 & -0.1 \\ -0.1 & i0.2 & 0.2 & -i0.1 \\ -i0.06 & -0.1 & i0.1 & 0.1 \end{pmatrix} \tag{2.11}$$

The resulting density matrix reflects that the population in the lowest energy level has been distributed into not only population and 1QC, but also into double quantum and triple quantum coherences (2QC and 3QC). 2QC and 3QC are coherent superposition states between energy eigenstates which differ in magnetic quantum number by 2 or 3. The matrix representation of these coherences is,

$$\begin{pmatrix} pop_{11} & 1QC_{12} & 2QC_{13} & 3QC_{14} \\ 1QC_{12} & pop_{22} & 1QC_{23} & 2QC_{24} \\ 2QC_{13} & 1QC_{23} & pop_{33} & 1QC_{34} \\ 3QC_{14} & 2QC_{24} & 1QC_{34} & pop_{44} \end{pmatrix}. \tag{2.12}$$

The evolution of the 2QC and 3QC is described using products of the Cartesian operators [32],

$$2QC_{xx} = \hbar\gamma Tr < I_x I_x \rho >, \tag{2.13}$$

$$3QC_{xxx} = \hbar\gamma Tr < I_x I_x I_x \rho > . \tag{2.14}$$

The physical interpretation of 2QC and 3QC is not as simple as the equation of 1QC and transverse magnetization. In particular, 2QC and 3QC cannot be detected directly using pulsed FT NMR since they are coherent superposition states between energy eigenstates differing in angular momentum by more than one, $\Delta m > 1$. Since photons carry $\hbar$ of angular momentum, only coherent superposition states differing by $\Delta m = 1$ are able to absorb or emit the single photon which interacts with the RF coil used in pulsed FT NMR experiments. It is possible to directly detect two and three photon transitions using continuous-wave NMR techniques with large RF power [31]. However, continuous-wave NMR techniques are much less useful than than pulsed FT NMR techniques. Indirect methods for the detection of MQC using pulsed FT NMR are discussed later in this chapter.

The first RF pulse applied to the isolated spin-3/2 system rotated the Boltzman distribution into only 1QC. In that example, the Boltzman distribution rotated into populations, 2QC, and 3QC canceled out. The canceling of these terms results from the exact balancing of excess and deficient population of the high temperature Boltzman distribution. The RF pulse applied to the unbalanced spin system rotated the spin population in the lowest energy eigenstate into all possible population and coherence states since there were not any spin population in the other energy eigenstates to cancel with it.

Canceling was also found with the 2nd RF rotation of the three 1QCs from the

isolated spin-3/2 system into the inverted population state. Consider the RF rotation of a system which has only 1QC between the middle two energy levels.

$$\frac{\hbar\gamma H_o}{kT}\begin{pmatrix} 0 & 0 & 0 & 0 \\ 0 & 0 & 1 & 0 \\ 0 & 1 & 0 & 0 \\ 0 & 0 & 0 & 0 \end{pmatrix} \xrightarrow{90^y} \frac{\hbar\gamma H_o}{kT}\begin{pmatrix} 0 & 0.4 & 0 & 0.6 \\ 0.4 & 0 & 0.2 & 0 \\ 0 & 0.2 & 0 & 0.4 \\ 0.6 & 0 & 0.4 & 0 \end{pmatrix} \tag{2.15}$$

In the previous isolated spin-3/2 example, the three 1QCs rotated into only population states. In this example we see that a single 1QC rotates into 3QC in addition to other 1QCs. Had we changed the phase of the initial 1QC or the RF pulse, the single 1QC would have been rotated into population states and 2QCs. The 2QCs or 3QC are not formed by the second RF pulse in the isolated spins example because of the balanced relationships of the magnitudes and phases of the three 1QCs.

The above examples show that in order to create MQC it is necessary to disrupt the magnitudes or phases of the three 1QCs in the interpulse period. One way to disrupt the phases between the three interpulse 1QCs is two apply a static electric field gradient (SEFG). The spin-3/2 ^{23}Na nuclei have a quadrupole moment Q which interacts with the SEFG. The quadrupole interaction produces a shift of the inner two Zeeman levels relative to the outer two Zeeman levels [29], see Figure 2.1.

The energy difference is increased between energy states 1 and 2 and decreased between energy states 3 and 4. If we apply a hard 90° Y-pulse, whose spectral profile is sufficiently broad to equally excite the increased 1,2 and decreased 3,4 transition frequencies, the spin-3/2 nuclei will again be rotated into $\rho = \frac{\hbar\gamma H_o}{kT} I_x$ [37]. Since the energy spacings are no longer the same, the three 1QCs are not going to precess at the same rate during the period t following the first pulse. The staggered precession of the three 1QCs in the density operator can be described in two parts [38]. The first term describes the evolution of the balanced part of the density matrix. The balanced part maintains the same phase and balanced magnitudes for all three 1QCs. The second term describes the evolution of the unbalanced part of the density matrix. The unbalanced part of the density matrix does not maintain the same phase or

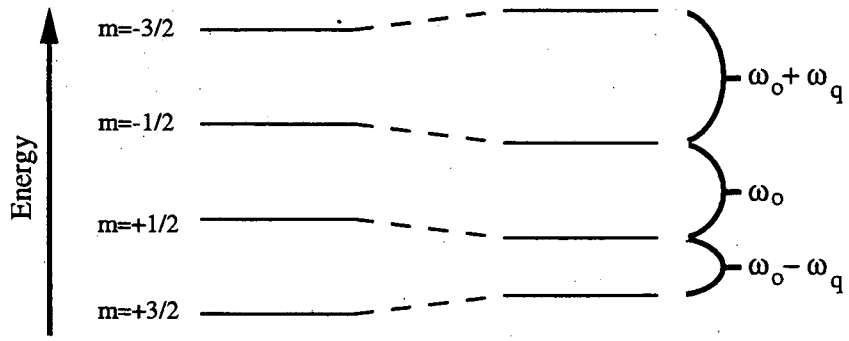

Figure 2.1: Shifting of spin-3/2 energy levels due to quadrupole interaction.

balance the magnitudes for the three 1QCs. The second part is referred to as the anti-phase term.

(2.16)

$$\frac{\hbar\gamma H_o}{kT}\begin{pmatrix} 0 & \frac{\sqrt{3}}{2} & 0 & 0 \\ \frac{\sqrt{3}}{2} & 0 & 1 & 0 \\ 0 & 1 & 0 & \frac{\sqrt{3}}{2} \\ 0 & 0 & \frac{\sqrt{3}}{2} & 0 \end{pmatrix}$$

$$\downarrow$$

Quadrupole Interaction

$$\downarrow$$

$$\frac{\hbar\gamma H_o}{kT}\left(\frac{3}{5}cos(\omega_Q t)+\frac{2}{5}\right)\begin{pmatrix} 0 & \frac{\sqrt{3}}{2} & 0 & 0 \\ \frac{\sqrt{3}}{2} & 0 & 1 & 0 \\ 0 & 1 & 0 & \frac{\sqrt{3}}{2} \\ 0 & 0 & \frac{\sqrt{3}}{2} & 0 \end{pmatrix}$$ Balanced 1QC

$$+$$

$$\frac{\hbar\gamma H_o}{kT}\begin{pmatrix} 0 & -\frac{2}{\sqrt{15}}(cos(\omega_Q t)-1) & 0 & 0 \\ & -\frac{\sqrt{5}}{2}sin(\omega_Q t) & & \\ -\frac{2}{\sqrt{15}}(cos(\omega_Q t)-1) & 0 & \frac{2}{\sqrt{5}}(cos(\omega_Q t)-1) & 0 \\ +\frac{\sqrt{5}}{2}sin(\omega_Q t) & & & \\ 0 & \frac{2}{\sqrt{5}}(cos(\omega_Q t)-1) & 0 & -\frac{2}{\sqrt{15}}(cos(\omega_Q t)-1) \\ & & & +\frac{\sqrt{5}}{2}sin(\omega_Q t) \\ 0 & 0 & -\frac{2}{\sqrt{15}}(cos(\omega_Q t)-1) & 0 \\ & & -\frac{\sqrt{5}}{2}sin(\omega_Q t) & \end{pmatrix}$$ Anti-Phase 1QC

The quadrupole shifted spins rotate differently under a second 90° pulse compared to the isolated spins in the previous example. The first term of the quadrupole shifted 1QC rotates into longitudinal magnetization as did the isolated spins.

(2.17)

$$\frac{\hbar\gamma H_o}{kT}\left(\frac{3}{5}cos(\omega_Q t)+\frac{2}{5}\right)\begin{pmatrix} 0 & \frac{\sqrt{3}}{2} & 0 & 0 \\ \frac{\sqrt{3}}{2} & 0 & 1 & 0 \\ 0 & 1 & 0 & \frac{\sqrt{3}}{2} \\ 0 & 0 & \frac{\sqrt{3}}{2} & 0 \end{pmatrix} \xrightarrow{90^y} \frac{\hbar\gamma H_o}{kT}\left(\frac{3}{5}cos(\omega_Q t)+\frac{2}{5}\right)\begin{pmatrix} \frac{3}{2} & 0 & 0 & 0 \\ 0 & \frac{1}{2} & 0 & 0 \\ 0 & 0 & -\frac{1}{2} & 0 \\ 0 & 0 & 0 & -\frac{3}{2} \end{pmatrix}$$

Balanced 1QC — Inverted Z-Magnetization

The anti-phase term is rotated into MQC since it does not have balanced phase and magnitude relationships between the three 1QCs.

(2.18)

$$\frac{\hbar\gamma H_o}{kT}\begin{pmatrix} 0 & -\frac{2}{\sqrt{15}}(cos(\omega_Q t)-1) & 0 & 0 \\ & -\frac{\sqrt{5}}{2}sin(\omega_Q t) & & \\ -\frac{2}{\sqrt{15}}(cos(\omega_Q t)-1) & 0 & \frac{2}{\sqrt{5}}(cos(\omega_Q t)-1) & 0 \\ +\frac{\sqrt{5}}{2}sin(\omega_Q t) & & & \\ 0 & \frac{2}{\sqrt{5}}(cos(\omega_Q t)-1) & 0 & -\frac{2}{\sqrt{15}}(cos(\omega_Q t)-1) \\ & & & +\frac{\sqrt{5}}{2}sin(\omega_Q t) \\ 0 & 0 & -\frac{2}{\sqrt{15}}(cos(\omega_Q t)-1) & 0 \\ & & -\frac{\sqrt{5}}{2}sin(\omega_Q t) & \end{pmatrix}$$ Anti-Phase 1QC

$$\downarrow 90^y$$

$$\begin{pmatrix} -\text{non-Boltzman pop} & 0 & \text{2QC term} & 0 \\ 0 & -\text{non-Boltzman pop} & 0 & \text{2QC term} \\ \text{2QC term} & 0 & \text{non-Boltzman pop} & 0 \\ 0 & \text{2QC term} & 0 & \text{non-Boltzman pop} \end{pmatrix}$$

The above approach to producing anti-phase 1QC used static quadrupole interactions to shift the Zeeman energy levels. Another approach to producing anti-phase coherence is by using asymmetric relaxation of the three 1QCs. How asymmetric quadrupole relaxation occurs in biological systems and how it gives rise to anti-phase 1QC and to MQC is discussed in next section.

2.2 Biological ^{23}Na and MQ Coherences

The environment of a biological ^{23}Na ion consists of a hydration shell surrounded by viscous biological media. Three interactions occur between the ^{23}Na nucleus and this environment. A dipole-dipole interaction occurs between the ^{23}Na nucleus and the dipole moments of the protons in the hydration sphere [4]. The quadrupole moment of the ^{23}Na nucleus interacts with the electric field gradients (EFGs) from the hydration sphere [39]. Finally, the ^{23}Na nuclear quadrupole moment interacts with EFGs from outside the hydration sphere [40, 4, 41, 17].

Knowledge of the strengths of these interactions enables us to determine which is the dominant interaction. The interaction between the ^{23}Na dipole moment μ_{na} and the proton dipolar magnetic field μ_p/r^3 produced by the hydration sphere is approximately,

$$H_{dd} = \mu_{na}\frac{\mu_p}{r^3}. \tag{2.19}$$

Taking the ^{23}Na dipole moment to be 10^{-23} erg/gauss and the dipole magnetic field strength to be 1 gauss at 1 angstrom from the proton, the dipole-dipole interaction is approximately 10^{-23} erg. Similarly the quadrupole interaction of the ^{23}Na quadrupole moment Q and the electric field gradient eq of the hydration shell may be estimated using [29],

$$H_Q = e^2QqSt\ . \tag{2.20}$$

Taking the ^{23}Na quadrupole moment to be 10^{-25}cm^2 , the hydration shell EFG to be $e10^{23}$cm^{-3}, and the Sternheimer term to be 5 [42], the quadrupole interaction is approximately 10^{-20} ergs. These two estimates show that the dipole-dipole interaction is insignificant compared to the quadrupole interaction.

As described in the previous section, the quadrupole interaction shifts the inner two energy states with respect to the outer two energy states. In contrast to the previous case where the energy levels were statically shifted, in this case the energy levels fluctuate randomly with time. The schematic below shows that these fluctuations vary the transition energy of the upper and lower transition, but not the middle

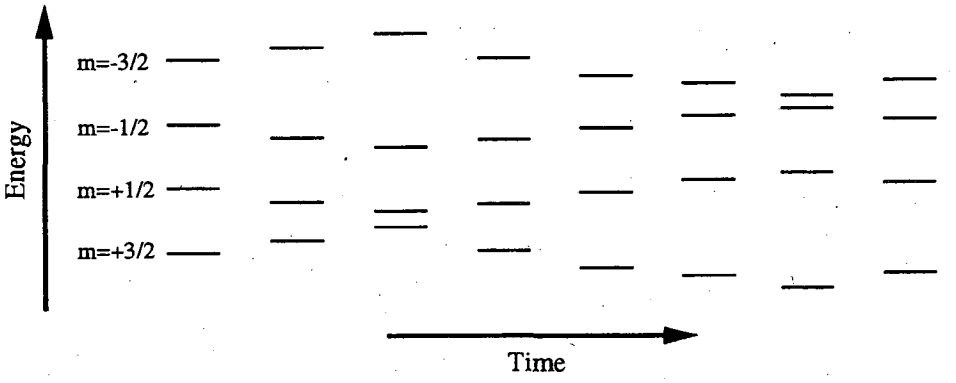

Figure 2.2: Fluctuations of spin-3/2 energy levels resulting from interactions between the nucleus of a ^{23}Na ion and electric field gradients produced by molecules in the surrounding environment.

transition, see Figure 2.2.

Using Redfield's theory of relaxation yields expressions for six ^{23}Na relaxation rates resulting from the quadrupole relaxation [43, 44, 29]. The two terms contributing to the relaxation rates are the quadrupole Hamiltonian H_Q and the assumed spectral density for the motion of the EFG with respect to the ion,

$$J(\omega) = \frac{\tau_c}{1 + (\omega\tau_c)^2}. \tag{2.21}$$

The six relaxation rates are

$$\frac{1}{T_{1s}} = \frac{H_Q^2}{10\hbar^2} J(2\omega), \tag{2.22}$$

$$\frac{1}{T_{1f}} = \frac{H_Q^2}{10\hbar^2} J(\omega), \tag{2.23}$$

$$\frac{1}{T_{2s}} = \frac{H_Q^2}{5\hbar^2}(J(\omega) + J(2\omega)), \tag{2.24}$$

$$\frac{1}{T_{2f}} = \frac{H_Q^2}{5\hbar^2}(J(0) + J(\omega)), \tag{2.25}$$

$$\frac{1}{T_{22}} = \frac{H_Q^2}{5\hbar^2}(J(0) + J(2\omega)), \tag{2.26}$$

$$\frac{1}{T_{23}} = \frac{H_Q^2}{5\hbar^2}(J(\omega) + J(2\omega)). \tag{2.27}$$

The $1/T_1$ rates determine the relaxation of the populations while the $1/T_2$ rates determine the relaxation of the 1Q, 2Q, and 3Q coherences, see Figure 2.3.

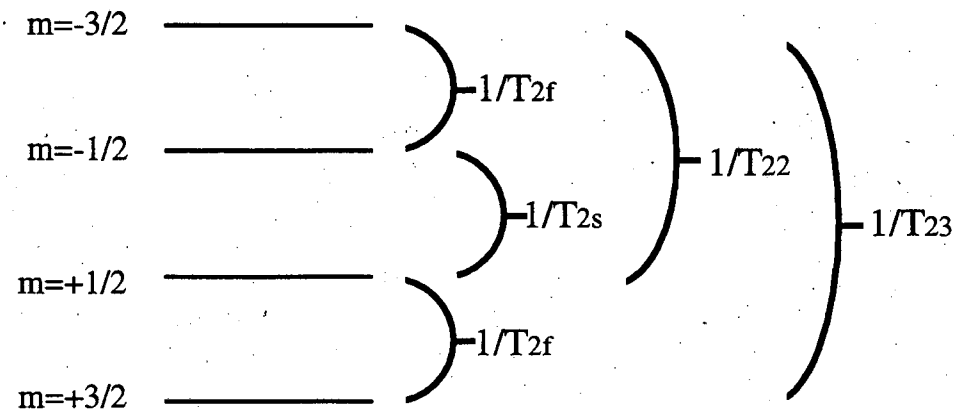

Figure 2.3: The relationships between the transverse relaxation rates and the coherence states.

If the correlation time of the EFG fluctuations is on the order of the Larmor precession time, then significant dephasing of the upper and lower 1QCs occurs. Significant dephasing of these coherences leads to a short T_{2f} relaxation time and a fast rate $1/T_{2f}$. Since the middle transition is not modulated, significant dephasing does not occur for this transition. The relaxation time T_{2s} is long which produces a slow rate $1/T_{2s}$. Thus the upper and lower 1QCs relaxation rate $1/T_{2f}$ is faster than the middle 1QC relaxation rate $1/T_{2s}$ [45].

If the correlation time of the EFG fluctuations are much faster than the Larmor precession time, then significant dephasing of the upper and lower 1QCs does not occur. The phenomenon of fast fluctuations producing little dephasing is referred to as motional narrowing [29]. Since there is not significant dephasing of the upper and lower 1QCs, their T_2 relaxation is the same as the middle 1QCs. Thus, for fast correlation times there is single-exponential T_2 relaxation, $T_{2f} = T_{2s}$ [46].

The Larmor precession time for a ^{23}Na nucleus in a 2.35 Tesla magnetic field is 4×10^{-8} sec. The typical correlation time for an EFG produced by the hydration shell is 10^{-12} sec [47]. These times indicate that ^{23}Na, which is relaxed primarily by its hydration shell, will have only one T_2 relaxation time. This relaxation time is

typically close to 50 ms. Therefore, ^{23}Na relaxed primarily by quadrupole interactions with its hydration shell is SER ^{23}Na. ^{23}Na ions that are diffusing near membranes or binding to large proteins interact with EFG whose correlation times are on the order of 10^{-8} sec [40, 4], producing two T_2 relaxation times. The fast relaxation time T_{2f} is on the order of 1 ms and the slow relaxation time T_{2s} is on the order of 20 ms . ^{23}Na relaxed by quadrupole interactions with large molecules is BER ^{23}Na.

An initial 90° RF pulse rotates equilibrium SER and BER ^{23}Na into transverse magnetization,

$$\rho = \frac{\hbar\gamma H_o}{kT}\begin{pmatrix} 0 & \frac{\sqrt{3}}{2} & 0 & 0 \\ \frac{\sqrt{3}}{2} & 0 & 1 & 0 \\ 0 & 1 & 0 & \frac{\sqrt{3}}{2} \\ 0 & 0 & \frac{\sqrt{3}}{2} & 0 \end{pmatrix}. \tag{2.28}$$

In an earlier example, it was shown that the magnitudes of the SER ^{23}Na 1QCs remain balanced during relaxation following the RF pulse. In contrast, the magnitudes of the BER ^{23}Na 1QCs do not remain balanced. This imbalance results in the density operator describing the relaxation of BER ^{23}Na consisting of a balanced term and an unbalanced anti-phase term,

(2.29)

$$\frac{\hbar\gamma H_o}{kT}\begin{pmatrix} 0 & \frac{\sqrt{3}}{2} & 0 & 0 \\ \frac{\sqrt{3}}{2} & 0 & 1 & 0 \\ 0 & 1 & 0 & \frac{\sqrt{3}}{2} \\ 0 & 0 & \frac{\sqrt{3}}{2} & 0 \end{pmatrix}$$

$$\downarrow$$

Biexponential Relaxation

$$\downarrow$$

$$\frac{\hbar\gamma H_o}{kT}\begin{pmatrix} 0 & \frac{\sqrt{3}}{2}e^{-t/T_{2f}} & 0 & 0 \\ \frac{\sqrt{3}}{2}e^{-t/T_{2f}} & 0 & e^{-t/T_{2s}} & 0 \\ 0 & e^{-t/T_{2s}} & 0 & \frac{\sqrt{3}}{2}e^{-t/T_{2f}} \\ 0 & 0 & \frac{\sqrt{3}}{2}e^{-t/T_{2f}} & 0 \end{pmatrix}$$

$$\|$$

$$\frac{\hbar\gamma H_o}{kT}\frac{3}{5}(e^{-t/T_{2f}} + \frac{2}{5}e^{-t/T_{2s}})\begin{pmatrix} 0 & \frac{\sqrt{3}}{2} & 0 & 0 \\ \frac{\sqrt{3}}{2} & 0 & 1 & 0 \\ 0 & 1 & 0 & \frac{\sqrt{3}}{2} \\ 0 & 0 & \frac{\sqrt{3}}{2} & 0 \end{pmatrix}$$ Balanced 1QC

$$+$$

$$\frac{\hbar\gamma H_o}{kT}\frac{\sqrt{6}}{5}(e^{-t/T_{2f}} - \frac{\sqrt{6}}{5}e^{-t/T_{2s}})\begin{pmatrix} 0 & -\frac{1}{\sqrt{2}} & 0 & 0 \\ -\frac{1}{\sqrt{2}} & 0 & \sqrt{\frac{3}{2}} & 0 \\ 0 & \sqrt{\frac{3}{2}} & 0 & -\frac{1}{\sqrt{2}} \\ 0 & 0 & -\frac{1}{\sqrt{2}} & 0 \end{pmatrix}$$ Anti-Phase 1QC

Applying a second 90° pulse to this system rotates the balanced term into longitudinal magnetization and the anti-phase term into MQC. The evolution of the BER ^{23}Na resembles the evolution of ^{23}Na interacting with a static EFG. In both cases anti-phase magnetization is produced in the interval between two RF pulses. However, BER ^{23}Na produces anti-phase magnetization due to imbalances in the magnitudes of the three 1QCs; while, ^{23}Na interacting with a static EFG produces anti-phase magnetization due to unequal phases among the three 1QCs. The magnitude imbalance among the three 1QCs results from quadrupole interactions with fluctuating EFGs.

2.3 Detecting MQ Coherences

2.3.1 Conventional Methods

In the first section of this chapter it was pointed out that two pulses are used to create a MQC. Unfortunately, the MQC cannot be detected directly using pulsed FT NMR. The invisibility of MQC results from their being superposition states between energy states that differ by more than one in angular momentum quantum number, $\Delta m > 1$. Since a single photon can only make transitions between energy levels with $\Delta m = 1$, a photon cannot be emitted by a MQC.

In order to detect the MQC it is necessary to use a third pulse. The third pulse converts the MQC back into a anti-phase 1QC, reversing the effect of the second pulse. Following the third pulse, the anti-phase 1QC evolves into balanced 1QC and may be detected by NMR. The difficulty with the experiment just described is that there is additional 1QC not produced by the MQC, see Figure 2.4. The challenge is to selectively detect 1QC generated from the MQC. One quantum coherence generated from multiple quantum coherence will be called M1QC. Other one quantum coherence generated from Z-magnetization or one quantum coherence will be called O1QC.

Since MQCs are between states with energy separation M times as large as for 1QCs, the MQCs precess M times faster than the 1QCs. A number of techniques take advantage of this fact to separate the M1QC from the O1QC. The first such technique, developed in 1976, separated M1QC and O1QC with two-dimensional spectroscopy [48]. Two-dimensional techniques collect multiple free induction decays as a function of the interpulse delay between the second and third RF pulses, see Figure 2.5. Stacking the FIDs on a grid yields the 1QC FID information on one axis, τ_1, and information on the evolution of the spins during the incremented interpulse on a second axis, τ_2. Performing a two-dimensional Fourier transform of the stacked FIDs yields a 2D spectrum [49, 50]. On such a spectrum the M1QCs are spectrally resolved from the O1QCs along the second axis since the MQCs precess M times faster than

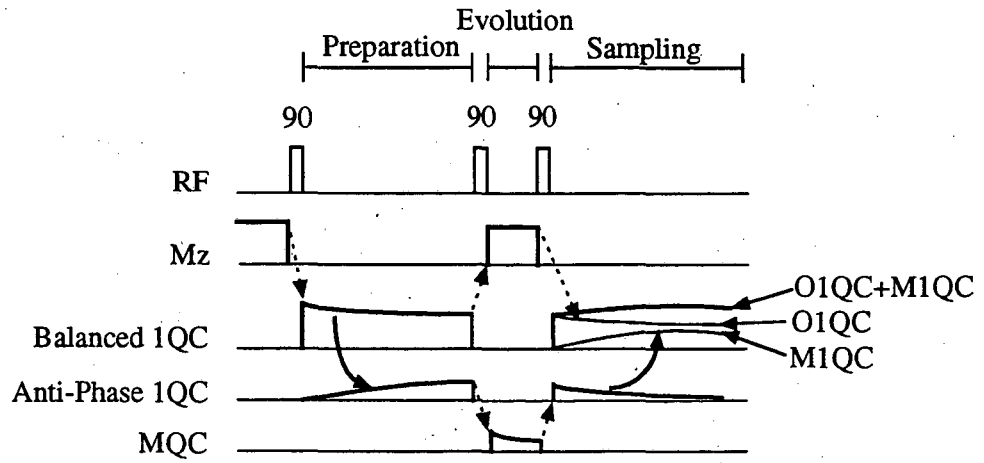

Figure 2.4: Three RF pulses produce one-quantum coherence resulting from multiple-quantum coherence pathways as well as from one-quantum coherence pathways and population pathways.

the 1QCs. The disadvantage of this technique is that it is very time consuming for systems with poor signal to noise.

The second approach, developed in 1980 [27], utilizes that the different precession rates of the MQC and the 1QC results in the MQC and the 1QC having different responses to changes of the phase of RF pulses. Consider how a 1QC and a 2QC respond to a 180 degree phase change in a RF pulse. A 90 degree pulse applied to a 1QC rotates it into Z-magnetization. A 180 degree phase change in the RF pulse changes the sign of the resulting Z-magnetization. A 90 degree pulse applied to a 2QC rotates it into anti-phase 1QC. It turns out that a 180 degree phase change in the 90 pulse does not change the sign of the anti-phase 1QC. However, a 90 degree phase change does change the sign of the resulting anti-phase 1QC. These phase changes are really rotations about the Z-axis. Above it is stated that MQCs precess M times more rapidly than 1QCs. Similarly, rotations about the Z-axis for MQCs are M times as large as for 1QCs. Thus, the 90 and 180 degree phase changes in the RF appear as 180 and 360 degree phase changes to the 2QC.

Using this intuition, let us examine the four pulse sequences $90_x, 90_x, 90_x$; 90_{-x}, 90_{-x}, 90_x; $90_y, 90_y, 90_x$; $90_{-y}, 90_{-y}, 90_x$, see Figure 2.6. In all four sequences the third

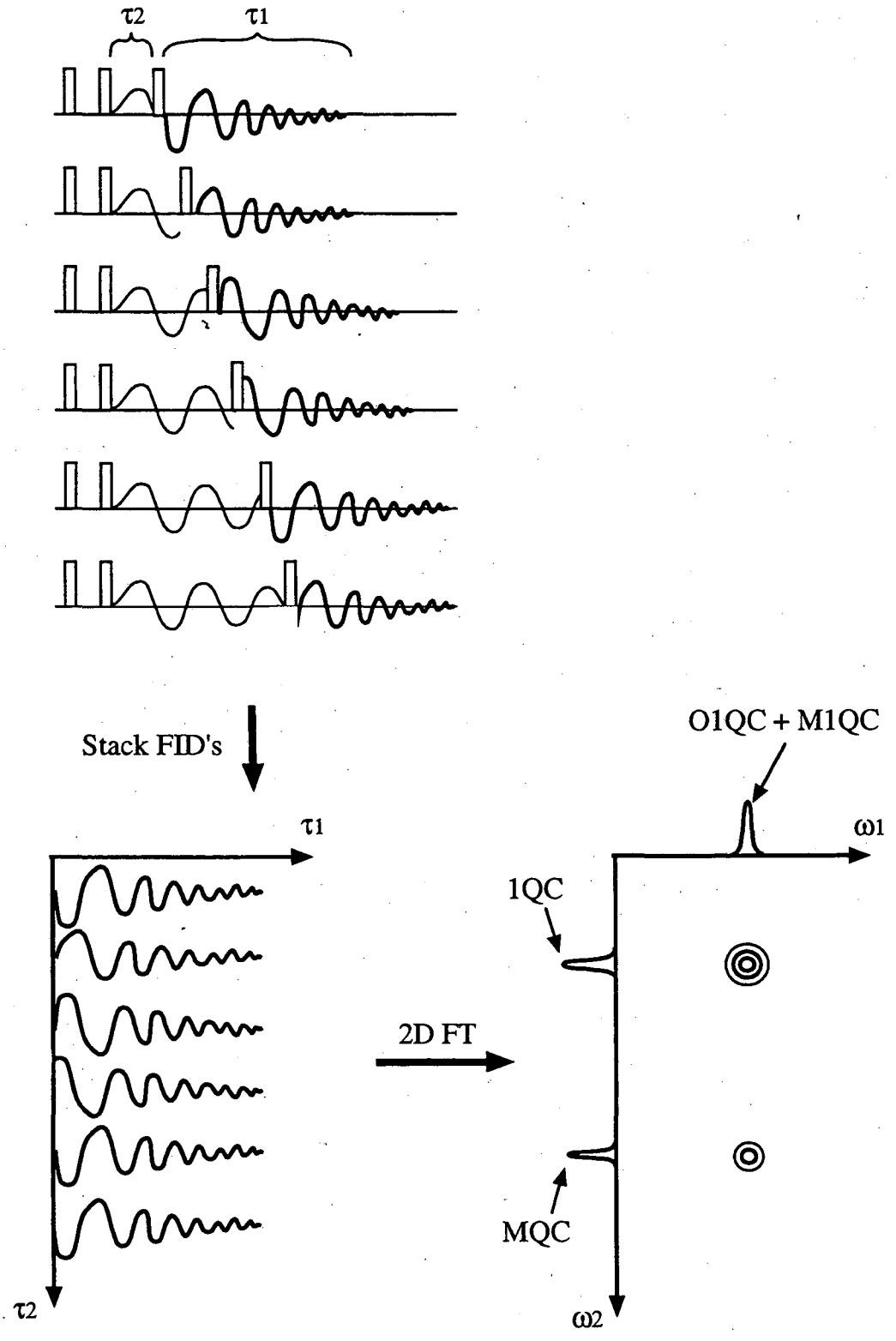

Figure 2.5: Two-dimensional spectroscopic method for detecting multiple-quantum coherences.

RF pulse converts -Mz into 01QC of the same phase. In contrast, the phases of the M1QC produced by sequences A and C in Figure 2.6 are shifted by 180° compared to the M1QC produced by sequences B and D. By adding the signal from A and C and subtracting the signal from B and D, (A+C-B-D), the O1QC is canceled and the M1QC is added. Figure 2.6 also shows how the O1QC resulting from T_1 relaxation during the preparation and evolution periods is canceled.

The disadvantage of phase-cycling techniques are that slight errors in the phase or flip angle of the RF pulses results in incomplete cancellation of the O1QC. The errors in phase and flip angle can be compensated for by using long phase-cycling protocols consisting of up to 64 steps. When implemented in imaging experiments, these large phase-cycling schemes usually produce prohibitively long imaging times.

The final approach to selectively detect M1QC, also developed in 1980 [51], uses gradients to dephase the O1QC signal, see figure 2.7. During the period between the second 90° RF pulse and the third 90° RF pulse a magnetic field gradient G is turned on for time t. In the presence of the gradient the 1QC dephases $\gamma G \Delta x t$, where Δx is the sample size. In contrast, the MQC dephases $M\gamma G \Delta x t$. The third 90° RF pulse converts the $M\gamma G \Delta x t$ dephased MQC into $M\gamma G \Delta x t$ dephased 1QC. By applying a second gradient after the third RF pulse for Mt, the M1QC rephases while any O1QC is dephased.

The major advantage of this technique is that it requires only a single three pulse sequence. The short duration of this sequence makes it feasible to perform MQ imaging in reasonable periods of time. A disadvantage of this technique is that the success of the gradient in dephasing unwanted signals is a function of the size of the sample. This gradient-selected technique yields poor suppression of signals for samples smaller than $2\pi/(\gamma G t)$. This drawback is not relevant for *in vivo* imaging of humans.

A second drawback of the gradient-selected technique is that it only detects half of the signal compared to the phase-cycled technique, see Figure 2.8. The explanation for this effect is found by examining the signal received from a 90-grad-90-grad pulse sequence compared to a 90-grad-180-grad pulse sequence. The first sequence rephases a tilted pancake of spins, while the second sequence rephases an inverted

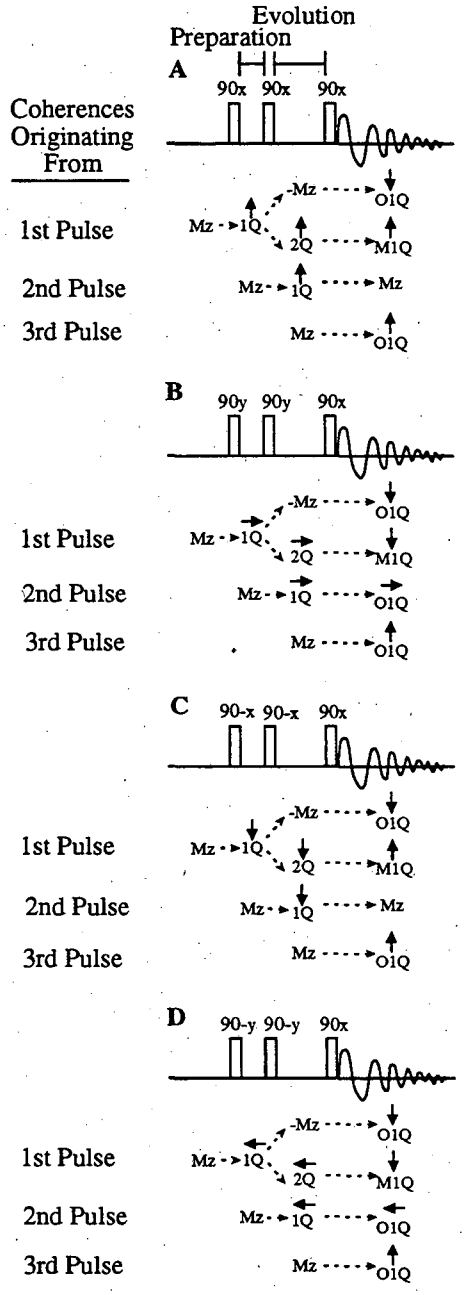

Coherences Originating From	Signal from A+C	Signal from B+D	Signal from A+C-B-D
1st Pulse (Mz)	$-M_z \rightarrow O_{1Q}$	$-M_z \rightarrow O_{1Q}$	0
1st Pulse (2Q)	$2Q \rightarrow M_{1Q}$	$2Q \rightarrow M_{1Q}$	$2Q \rightarrow M_{1Q}$
2nd Pulse	0	0	0
3rd Pulse	$M_z \rightarrow O_{1Q}$	$M_z \rightarrow O_{1Q}$	0

Figure 2.6: Phase-cycled method for detecting multiple-quantum coherences.

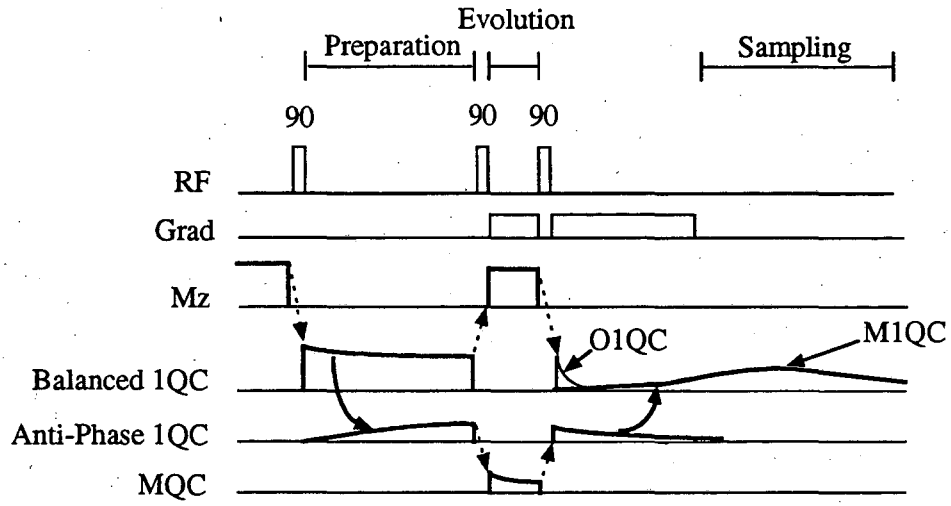

Figure 2.7: Gradient-selected method for detecting multiple-quantum coherences.

pancake of spins. The refocusing of the tilted pancake leaves half of the available magnetization aligned as undetectable longitudinal magnetization. The refocusing of the inverted pancakes converts all of the available magnetization into detectable transverse magnetization. The GSMQ filter loses half of its signal in the same manner as the 90-grad-90-grad sequence.

2.3.2 Modified GS3Q Filter

A modified GS3Q filter for imaging BER ^{23}Na in the human brain is presented here. The modified GS3Q filter is designed to do three things: 1) take advantage of increased MQ SNR found at short repetition times, 2) suppress increased spurious 1Q signals which occur at short repetition times, and 3) require a small number of phase cycling steps so that three dimensional imaging may be performed. The modified

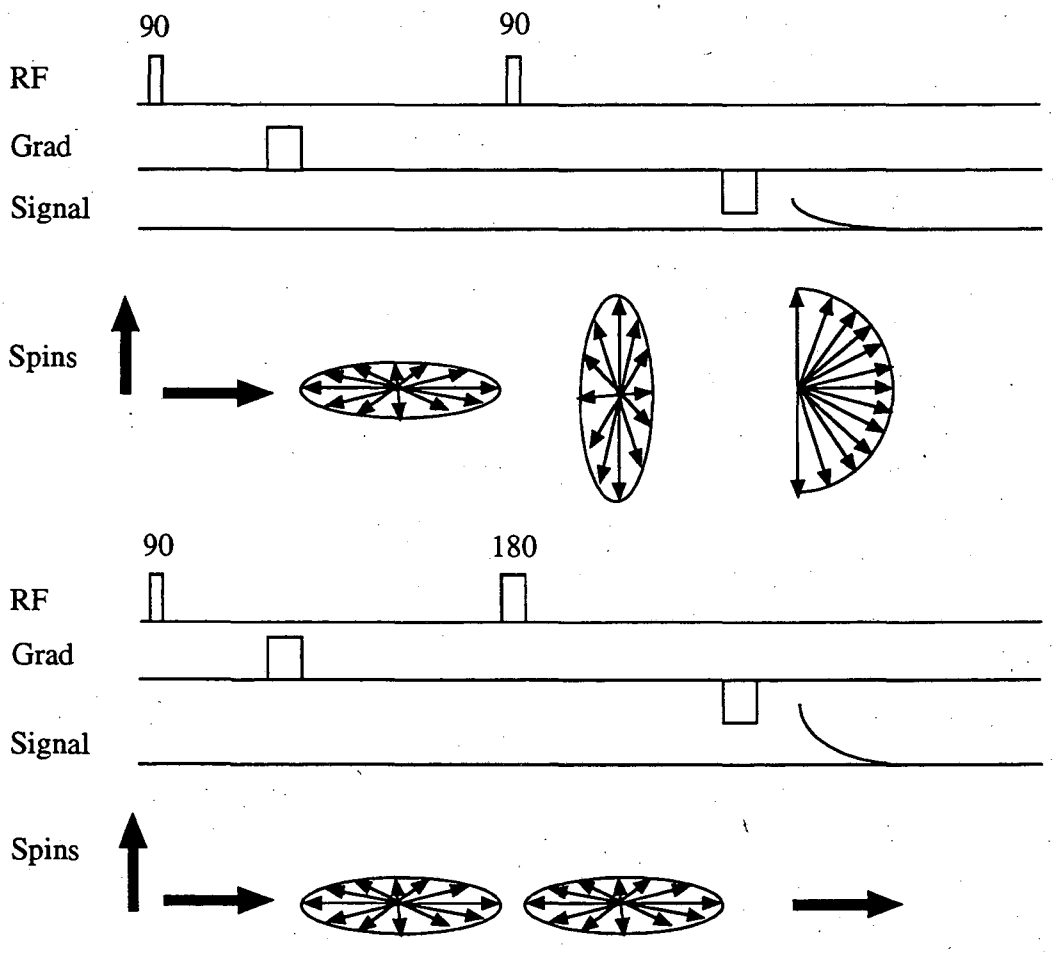

Figure 2.8: The upper 90,90 sequence produces half of the signal of the lower 90,180 sequence. The gradient-selected multiple-quantum filter loses half of its signal in the same manner as does the upper 90,90 sequence.

GS3Q filter incorporates elements from both gradient-selected and phase-cycling MQ filtering techniques as well as a preparatory crusher gradient.

Calculations and experimental results are presented in Chapter 4 which show that for a fixed experimental time the GS3Q ^{23}Na SNR increases by a factor of two as the repetition time decreases from 300 ms to 55 ms for ^{23}Na in a 4% agarose gel. Additional calculations and experimental results are presented in Chapter 4 which show that for decreased repetition times the amount of spurious 1Q signals also increases. Therefore, increasing the GS3Q filtered ^{23}Na SNR by reducing the repetition time is limited by how well the GS3Q filter suppresses spurious 1Q signals. The suppression can be improved at short repetition times by modifying the GS3Q filter with the addition of a preparatory crusher gradient and two-step-phase cycling. The preparatory crusher gradient helps to dephase transverse magnetization [52, 53] so predominantly Z-magnetization remains for the subsequent 3Q filter. Two-step-phase cycling is employed to provide partial subtraction of 1QC signals while adding 3QC signals.

The modified GS3Q filter sequence incorporating a preparatory crusher gradient and two-step-phase cycling is displayed in Figure 2.9. The first, third, fourth, fifth, seventh, and eighth RF pulses are 90° pulses. The second and sixth RF pulses are 180° refocusing pulses. The G_{3Q} gradient is in the X direction, while the crusher gradient is in the Z direction. Other parameters for the modified GS3Q filter are discussed in Section 4.2.

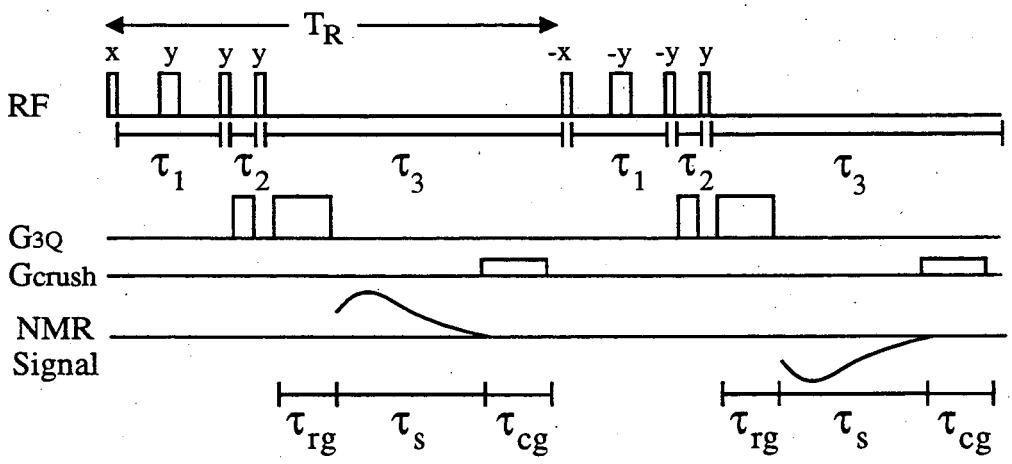

Figure 2.9: Schematic representation of the modified gradient-selected triple-quantum filter with preparatory crusher gradient and two-step-phase cycling. See Table 4.2 for other parameters.

Chapter 3

Calculations for GS3Q Filter

In this chapter the magnitude of the signals from the modified and conventional gradient-selected 3Q filters are calculated for various repetition times and resonance offsets. These calculations are simplified by using the superoperator formalism and the irreducible spherical operator representation of the spin-3/2 density operator. In Section 3.1, the superoperator formalism is reviewed. In Section 3.2, the properties of the irreducible spherical tensors are reviewed. In Section 3.3, an evolution equation for ^{23}Na is formulated. In Section 3.4, the evolution equation is used in calculations solving for the modified and conventional GS3Q filter signal to noise ratio, suppression factor, and spurious ratio.

3.1 Superoperator Formalism

As mentioned in Chapter 2, the equation of motion for the density operator is

$$\frac{d\rho}{dt} = i[\rho, H], \tag{3.1}$$

and the evolution equation is

$$\rho(t) = e^{-iHt}\rho(0)e^{iHt}. \tag{3.2}$$

A rearrangement of the presentation of the density operator significantly simplifies both the dynamical equation and the evolution equation [30]. This formulation defines new superoperators which act upon the density operator. In the superoperator formulation, the density operator is represented as a n x 1 column vector and the operators are represented as n x n matrices. Any operation of a superoperator upon the density operator is a simple matrix multiplication between a matrix and a vector. The single matrix multiplication with a superoperator is significantly easier to calculate compared to the conventional commutation and rotation operations. The physical significance of individual elements of the superoperators are also easier to determine than with conventional operators. Each element of a superoperator explicitly connects two elements of the density operator. This is not the case with conventional operators.

The three basic superoperators are a commutation superoperator, a rotation superoperator, and a relaxation superoperator. The commutation and rotation superoperators are found by multiplying out the conventional matrix commutation and rotation operations and then separating the superoperator tensor and density operator vector by inspection. The relaxation superoperator is found using Redfield's theory of relaxation [43, 29].

To see how the superoperator rearrangement is performed, the unitary transformation for a spin-1/2 nuclei will be examined. The unitary operation is between the operator B and the density operator ρ. Explicitly evaluating the unitary operation and rearranging terms leads to a single matrix multiplication between a new 4x4 tensor operator and the rearranged 4x1 density operator,

$$\begin{pmatrix} B_{11} & B_{12} \\ B_{21} & B_{22} \end{pmatrix} \begin{pmatrix} \rho_{11} & \rho_{12} \\ \rho_{21} & \rho_{22} \end{pmatrix} \begin{pmatrix} B_{11} & B_{12} \\ B_{21} & B_{22} \end{pmatrix}^t$$

$$\| $$

$$\begin{pmatrix} B_{11} & B_{12} \\ B_{21} & B_{22} \end{pmatrix} \begin{pmatrix} \rho_{11}B_{11}^t + \rho_{12}B_{21}^t & \rho_{11}B_{12}^t + \rho_{12}B_{22}^t \\ \rho_{21}B_{11}^t + \rho_{22}B_{21}^t & \rho_{21}B_{11}^t + \rho_{22}B_{21}^t \end{pmatrix}$$

$$\| $$

$$\begin{pmatrix} B_{11}\rho_{11}B_{11}^t + B_{11}\rho_{12}B_{21}^t + B_{12}\rho_{21}B_{12}^t & B_{11}\rho_{11}B_{22}^t + B_{11}\rho_{12}B_{22}^t + B_{12}\rho_{21}B_{11}^t \\ \quad + B_{12}\rho_{22}B_{21}^t & \quad + B_{12}\rho_{22}B_{21}^t \\ B_{21}\rho_{11}B_{11}^t + B_{21}\rho_{12}B_{21}^t + B_{22}\rho_{21}B_{12}^t & B_{21}\rho_{11}B_{22}^t + B_{21}\rho_{12}B_{22}^t + B_{22}\rho_{21}B_{11}^t \\ \quad + B_{22}\rho_{22}B_{21}^t & \quad + B_{22}\rho_{22}B_{21}^t \end{pmatrix}$$

$$\downarrow$$

$$\begin{pmatrix} B_{11}\rho_{11}B_{11}^t + B_{11}\rho_{12}B_{21}^t + B_{12}\rho_{21}B_{11}^t + B_{12}\rho_{22}B_{21}^t \\ B_{21}\rho_{11}B_{12}^t + B_{21}\rho_{12}B_{22}^t + B_{22}\rho_{21}B_{12}^t + B_{22}\rho_{22}B_{22}^t \\ B_{11}\rho_{11}B_{12}^t + B_{11}\rho_{12}B_{22}^t + B_{12}\rho_{21}B_{12}^t + B_{12}\rho_{22}B_{22}^t \\ B_{21}\rho_{11}B_{11}^t + B_{21}\rho_{12}B_{21}^t + B_{22}\rho_{21}B_{11}^t + B_{22}\rho_{22}B_{21}^t \end{pmatrix}$$

$$\| $$

$$\begin{pmatrix} B_{11}B_{11}^t & B_{11}B_{21}^t & B_{12}B_{11}^t & B_{12}B_{21}^t \\ B_{21}B_{12}^t & B_{21}B_{22}^t & B_{22}B_{12}^t & B_{22}B_{22}^t \\ B_{11}B_{12}^t & B_{11}B_{22}^t & B_{12}B_{12}^t & B_{12}B_{22}^t \\ B_{21}B_{11}^t & B_{21}B_{21}^t & B_{22}B_{11}^t & B_{22}B_{21}^t \end{pmatrix} \begin{pmatrix} \rho_{11} \\ \rho_{12} \\ \rho_{21} \\ \rho_{22} \end{pmatrix}$$

The final 4x4 tensor may be used to convert any 2x2 rotation operator into a rotation superoperator.

To see how the commutation superoperator rearrangement is performed, let us examine commutation between a spin-1/2 density operator and a Hamiltonian. Explicitly evaluating the commutation operation and rearranging terms leads to a single matrix multiplication between a new 4x4 commutation superoperator and a

rearranged 4x1 density operator.

$$\left[\begin{pmatrix} \rho_{11} & \rho_{12} \\ \rho_{21} & \rho_{22} \end{pmatrix}, \begin{pmatrix} h_{11} & h_{12} \\ h_{21} & h_{22} \end{pmatrix}\right]$$

$$\| $$

$$\begin{pmatrix} \rho_{11} & \rho_{12} \\ \rho_{21} & \rho_{22} \end{pmatrix}\begin{pmatrix} h_{11} & h_{12} \\ h_{21} & h_{22} \end{pmatrix} - \begin{pmatrix} h_{11} & h_{12} \\ h_{21} & h_{22} \end{pmatrix}\begin{pmatrix} \rho_{11} & \rho_{12} \\ rho_{21} & \rho_{22} \end{pmatrix}$$

$$\| $$

$$\begin{pmatrix} \rho_{11}h_{11}+\rho_{12}h_{21} & \rho_{11}h_{12}+\rho_{12}h_{22} \\ \rho_{21}h_{11}+\rho_{22}h_{21} & \rho_{21}h_{12}+\rho_{22}h_{22} \end{pmatrix} - \begin{pmatrix} h_{11}\rho_{11}+h_{12}\rho_{21} & h_{12}\rho_{12}+h_{12}\rho_{22} \\ h_{21}\rho_{11}+h_{22}\rho_{21} & h_{21}\rho_{12}+h_{22}\rho_{22} \end{pmatrix}$$

$$\| $$

$$\begin{pmatrix} \rho_{12}h_{21}-h_{12}\rho_{21} & \rho_{11}h_{11}+\rho_{12}h_{21}-h_{11}\rho_{12}-h_{12}\rho_{22} \\ \rho_{21}h_{11}+\rho_{22}h_{21}-h_{21}\rho_{11}-h_{22}\rho_{21} & \rho_{21}h_{12}+\rho_{12}h_{21} \end{pmatrix}$$

$$\downarrow$$

$$\begin{pmatrix} \rho_{12}h_{21}-h_{12}\rho_{21} \\ \rho_{11}h_{11}+\rho_{12}h_{21}-h_{11}\rho_{12}-h_{12}\rho_{22} \\ \rho_{21}h_{11}+\rho_{22}h_{21}-h_{21}\rho_{11}-h_{22}\rho_{21} \\ \rho_{21}h_{12}+\rho_{12}h_{21} \end{pmatrix}$$

$$\| $$

$$\begin{pmatrix} 0 & h_{21} & -h_{12} & 0 \\ h_{11} & h_{21}-h_{21} & 0 & -h_{12} \\ -h_{21} & 0 & h_{11}-h_{22} & h_{21} \\ 0 & h_{21} & h_{12} & 0 \end{pmatrix}\begin{pmatrix} \rho_{11} \\ \rho_{12} \\ \rho_{21} \\ \rho_{22} \end{pmatrix}$$

One advantage of the superoperator formulation is that the rotation operation involves fewer multiplications. Using conventional operators, the multiplications performed to create the rotation superoperator would need to be repeated each time a rotation operation is performed. In the superoperator formalism the multiplications used to form the superoperator are only performed once. In the next section it is shown that the superoperator formulation provides significant intuitive insight into the dynamics of the spin system.

3.2 Irreducible Representation of Density Matrix

The density operator for spin-1/2 systems can be represented as a linear combination of the operators $I_x, I_y, \text{and}, I_z$,

$$\rho = c_1 I_x + c_2 I_y + c_3 I_z. \tag{3.3}$$

However, the three operators $I_x, I_y, \text{and}, I_z$ do not span all the possible states of the spin-3/2 density operator. To span the density operator space it is necessary to use products of the operators $I_x, I_y, \text{and}, I_z$ [32]. These include $I_x I_x, I_x I_y, I_x I_z$, etc. In all there are sixteen product operators which form a basis for the spin-3/2 density operator. The product operators are a convenient basis for the density operator since they are formed with the familiar Cartesian operators $I_x, I_y, \text{and}, I_z$. Unfortunately, the rotation properties of the product operators are cumbersome [32].

Another set of operators which have less cumbersome rotation properties are the irreducible spherical operators, T_{lm} [54, 55, 56]. The simplified rotation properties of the T_{lm} operators results from their grouping into different ranks l. Groups of operators with the same rank rotate with the same properties: l=0 are scalars, l=1 are vectors, l=2 are second rank tensors, etc. T_{lm} of a certain rank are only rotated into other T_{lm} of the same rank. The rank can only change during the evolution periods between RF pulses.

The order m denotes the various kinds of operators which exist within each rank [38]. If the order of an operator is zero, then it represents a population state. If the order of an operator is greater than one, then it represents a coherent superposition state between two states differing in magnetic quantum number by the order number. The order can only change during an RF rotation.

The T_{lm} are proportional to the spherical harmonic functions $Y_{lm}(\theta, \phi)$. As with the $Y_{lm}(\theta, \phi)$ functions, the T_{lm} operators may be related to the Cartesian operators, see Table 3.1. Rank zero operators are the identity operator and rank one operators are simple combinations of the Cartesian operators. Note that order $m = 0$ denotes longitudinal magnetization and $m = \pm 1$ denotes transverse magnetization, or 1st

order coherence.

TABLE 3.1

Irreducible Operators Relationships to Cartesian Operators

Irreducible Operator	Cartesian Operators
T_{00}	1
T_{10}	I_z
$T_{1(\pm1)}$	$\mp\frac{1}{\sqrt{2}}(I_\pm = I_x \pm iI_y)$

The T_{lm} with rank greater than one are related to products of the Cartesian operators, see Table 3.2. The rank 2 and rank 3 operators describe non-Boltzman population distributions, anti-phase 1QC, 2QC, and 3QC. The 0th order operators describe non-Boltzmann population distributions. The 1st order operators describe anti-phase 1QC. The 2nd and 3rd order operators describe 2QC and 3QC.

TABLE 3.2

Irreducible Operators Relationships to Products of Cartesian Operators

Irreducible Operator	Cartesian Operators
T_{20}	$\frac{1}{\sqrt{6}}(3I_z^2 - I(I+1))$
$T_{2(\pm1)}$	$\mp\frac{1}{2}[I_z, I_\pm]_+$
$T_{2(\pm2)}$	$\frac{1}{2}I_\pm^2$
T_{30}	$\frac{1}{\sqrt{10}}(5I_z^3 - (3I(I+1)-1)I_z)$
$T_{3(\pm1)}$	$\mp\sqrt{\frac{3}{160}}[(5I_z^2 - 3I(I+1) - \frac{1}{2}), I_\pm]_+$
$T_{3(\pm2)}$	$\mp\sqrt{\frac{3}{16}}[I_z, I_\pm^2]_+$
$T_{3(\pm3)}$	$\frac{1}{2\sqrt{2}}I_\pm^3$

3.3 Evolution Equation

Using a superoperator rotation matrix $R(\beta,\phi)$ and superoperator quadrupolar relaxation matrix $U(t,\delta\omega)$ it is possible to formulate an equation describing the action of a radio frequency (RF) hard pulse upon the spin-3/2 density operator ρ followed by quadrupole relaxation,

$$\rho(t) = U(t,\delta\omega)R(\beta,\phi)\rho(0) + G(t). \tag{3.4}$$

This evolution equation is similar in form to solutions for the Bloch equation. It is easier to work with this evolution equation compared to conventional evolution equations which use unitary operations to evaluate the effect of the RF pulse.

The superoperator representation of the density operator in the above evolution equation is a vector,

$$\rho = [\rho_{00},\rho_{11},\rho_{10},\rho_{1(-1)},\rho_{22},\rho_{21},\rho_{20},\rho_{2(-1)},\rho_{2(-2)},\rho_{33},\rho_{32},\rho_{31},\rho_{30},\rho_{3(-1)},\rho_{3(-2)},\rho_{3(-3)}]^T. \tag{3.5}$$

The elements of the vector are the coefficients for a linear expansion of the density operator in terms of the irreducible spherical operators,

$$\rho = \rho_{00}T_{00} + \rho_{11}T_{11} + \rho_{10}T_{10} + \rho_{1(-1)}T_{1(-1)} + \rho_{22}T_{22} + \dots . \tag{3.6}$$

The vector $G(t)$ describes the relaxation of the Z-magnetization towards the thermal equilibrium magnetization,

$$G(t) = [0,0,d(1-C_{22}(t)),0,0,0,0,0,0,0,0,0,-dE_{22}(t),0,0,0]^T, \tag{3.7}$$

where the density operator description of ^{23}Na nuclei in thermal equilibrium is

$$\rho_{eq} = [0,0,d,0,0,0,0,0,0,0,0,0,0,0,0,0]^T. \tag{3.8}$$

The rotation superoperator $R(\beta,\phi)$ describing the rotation $r(\beta,\phi)$ of the T_{lm} operator is found using the rotation rule [55],

$$r(-\phi,\beta,\phi)T_{lm}r^{-1}(-\phi,\beta,\phi) = \sum_{m'} T_{lm'}e^{-i(m-m')\phi}d^l_{mm'}(\beta) \tag{3.9}$$

where $-\phi, \beta, \phi$ are Euler angles and $d^l_{mm'}(\beta)$ is a reduced Wigner rotation element. Using this expression the rotation superoperator $R(\beta, \phi)$ with flip angle β and phase ϕ is found to have block diagonal form,

$$R(\beta,\phi)=\begin{bmatrix} {}^0R_{ij}(\beta,\phi) & 0 & 0 & 0 \\ 0 & {}^1R_{ij}(\beta,\phi) & 0 & 0 \\ 0 & 0 & {}^2R_{ij}(\beta,\phi) & 0 \\ 0 & 0 & 0 & {}^3R_{ij}(\beta,\phi) \end{bmatrix}.$$

The matrix ${}^0R_{ij}(\beta, \phi)$ has dimensions 1×1, the matrix ${}^1R_{ij}(\beta, \phi)$ has dimensions 3×3, the matrix ${}^2R_{ij}(\beta, \phi)$ has dimensions 5×5, and the matrix ${}^3R_{ij}(\beta, \phi)$ has dimensions 7×7. Each ${}^lR_{ij}(\beta, \phi)$ is responsible for the rotation of the group of irreducible operators of a rank l into irreducible operators of the same rank. The block diagonal form of $R(\beta, \phi)$ explicitly shows that irreducible operators of different rank cannot be rotated into each other. It is shown below that the elements of ${}^0R_{ij}(\beta, \phi)$ and ${}^2R_{ij}(\beta, \phi)$ are not needed in this analysis. The elements of ${}^1R_{ij}(\beta, \phi)$ and ${}^3R_{ij}(\beta, \phi)$ are listed in Table 3.3. For rank $l = 1$, the transverse magnetization $T_{1\pm1}$ is rotated into longitudinal magnetization T_{10} and vice versa. For rank $l = 3$, anti-phase magnetization $T_{3\pm1}$ is rotated into non-equilibrium population (T_{30}), 2QC ($T_{3\pm2}$), 3QC ($T_{3\pm3}$) and vice versa.

TABLE 3.3

Elements of Rotation Matrix $R_{ij}(\beta,\phi)$

Matrix Elements	Value
${}^1R_{11}(\beta,\phi)$,${}^1R_{33}(\beta,\phi)$	$\cos^2\frac{\beta}{2}$
${}^1R_{22}(\beta,\phi)$	$\cos\beta$
${}^1R^*_{21}(\beta,\phi)$,${}^1R^*_{32}(\beta,\phi)$,$-{}^1R_{12}(\beta,\phi)$,$-{}^1R_{23}(\beta,\phi)$	$e^{i\phi}\frac{1}{\sqrt{2}}\sin\beta$
${}^1R^*_{31}(\beta,\phi)$,${}^1R_{13}(\beta,\phi)$	$e^{2i\phi}\sin^2\frac{\beta}{2}$
${}^3R_{11}(\beta,\phi)$,${}^3R_{77}(\beta,\phi)$	$\cos^6\frac{\beta}{2}$
$-{}^3R^*_{12}(\beta,\phi)$,$-{}^3R^*_{67}(\beta,\phi)$,${}^3R_{21}(\beta,\phi)$,${}^3R_{76}(\beta,\phi)$	$e^{i\phi}\sqrt{6}\cos^5\frac{\beta}{2}\sin\frac{\beta}{2}$
${}^3R^*_{13}(\beta,\phi)$,${}^3R^*_{57}(\beta,\phi)$,${}^3R_{31}(\beta,\phi)$,${}^3R_{75}(\beta,\phi)$	$e^{2i\phi}\frac{\sqrt{15}}{8}\sin^2\beta(1+\cos\beta)$
$-{}^3R^*_{14}(\beta,\phi)$,$-{}^3R^*_{47}(\beta,\phi)$,${}^3R_{41}(\beta,\phi)$,${}^3R_{74}(\beta,\phi)$	$e^{3i\phi}\frac{\sqrt{5}}{4}\sin^3\beta$
${}^3R^*_{15}(\beta,\phi)$,${}^3R^*_{37}(\beta,\phi)$,${}^3R_{51}(\beta,\phi)$,${}^3R_{73}(\beta,\phi)$	$e^{4i\phi}\frac{\sqrt{15}}{8}\sin^2\beta(1-\cos\beta)$
$-{}^3R^*_{16}(\beta,\phi)$,$-{}^3R^*_{27}(\beta,\phi)$,${}^3R_{61}(\beta,\phi)$,${}^3R_{72}(\beta,\phi)$	$e^{5i\phi}\sqrt{6}\sin^5\frac{\beta}{2}\cos\frac{\beta}{2}$
${}^3R^*_{17}(\beta,\phi)$,${}^3R_{71}(\beta,\phi)$	$e^{6i\phi}\sin^6\frac{\beta}{2}$
${}^3R_{22}(\beta,\phi)$,${}^3R_{66}(\beta,\phi)$	$\frac{1}{4}(1+\cos\beta)^2(3\cos\beta-2)$
${}^3R^*_{23}(\beta,\phi)$,${}^3R^*_{56}(\beta,\phi)$,$-{}^3R_{32}(\beta,\phi)$,$-{}^3R_{65}(\beta,\phi)$	$e^{i\phi}\frac{\sqrt{10}}{8}\sin\beta(1-3\cos\beta)(\cos\beta+1)$
${}^3R^*_{24}(\beta,\phi)$,${}^3R^*_{46}(\beta,\phi)$,${}^3R_{42}(\beta,\phi)$,${}^3R_{64}(\beta,\phi)$	$e^{2i\phi}\sqrt{\frac{15}{8}}\sin^2\beta\cos\beta$
${}^3R^*_{25}(\beta,\phi)$,${}^3R^*_{36}(\beta,\phi)$,$-{}^3R_{52}(\beta,\phi)$,$-{}^3R_{63}(\beta,\phi)$	$e^{3i\phi}\frac{\sqrt{10}}{8}\sin\beta(1+3\cos\beta)(\cos\beta-1)$
${}^3R^*_{26}(\beta,\phi)$,${}^3R_{62}(\beta,\phi)$,	$e^{4i\phi}\frac{1}{4}(1-\cos\beta)^2(3\cos\beta+2)$
${}^3R_{33}(\beta,\phi)$,${}^3R_{55}(\beta,\phi)$	$\frac{1}{8}(1+\cos\beta)(15\cos^2\beta-10\cos\beta-1)$
$-{}^3R^*_{34}(\beta,\phi)$,$-{}^3R^*_{45}(\beta,\phi)$,${}^3R_{43}(\beta,\phi)$,${}^3R_{54}(\beta,\phi)$	$e^{i\phi}\frac{\sqrt{3}}{4}\sin\beta(5\cos^2\beta-1)$
${}^3R^*_{35}(\beta,\phi)$,${}^3R_{53}(\beta,\phi)$	$e^{2i\phi}\frac{1}{8}(1-\cos\beta)(15\cos^2\beta+10\cos\beta-1)$
${}^3R_{44}(\beta,\phi)$	$\frac{1}{2}\cos\beta(5\cos^2\beta-3)$

In contrast to rotation which occurs between operators of the same rank, the relaxation operation produces transitions between irreducible operators of different rank but the same order. The superoperator describing quadrupole relaxation is determined using Redfield's theory of relaxation [43, 29, 57, 44]. In contrast with the rotation matrix, the quadrupole relaxation matrix $U(t,\delta\omega)$ does not have block diagonal form:

$$U(t,\delta\omega) =$$

$$\begin{pmatrix}
0 & 0 & 0 & 0 & 00000 & 0 & 0 & 0 & 0 & 0 & 0 & 0 \\
0 & C_{11}(t,\delta\omega) & 0 & 0 & 00000 & 0 & 0 & D_{11}(t,\delta\omega) & 0 & 0 & 0 & 0 \\
0 & 0 & C_{22}(t) & 0 & 00000 & 0 & 0 & 0 & D_{22}(t) & 0 & 0 & 0 \\
0 & 0 & 0 & C_{33}(t,\delta\omega) & 00000 & 0 & 0 & 0 & 0 & D_{33}(t,\delta\omega) & 0 & 0 \\
0 & 0 & 0 & 0 & 00000 & 0 & 0 & 0 & 0 & 0 & 0 & 0 \\
0 & 0 & 0 & 0 & 00000 & 0 & 0 & 0 & 0 & 0 & 0 & 0 \\
0 & 0 & 0 & 0 & 00000 & 0 & 0 & 0 & 0 & 0 & 0 & 0 \\
0 & 0 & 0 & 0 & 00000 & 0 & 0 & 0 & 0 & 0 & 0 & 0 \\
0 & 0 & 0 & 0 & 00000 & 0 & 0 & 0 & 0 & 0 & 0 & 0 \\
0 & 0 & 0 & 0 & 00000 & F_{11}(t,\delta\omega) & 0 & 0 & 0 & 0 & 0 & 0 \\
0 & 0 & 0 & 0 & 00000 & 0 & F_{22}(t,\delta\omega) & 0 & 0 & 0 & 0 & 0 \\
0 & E_{11}(t,\delta\omega) & 0 & 0 & 00000 & 0 & 0 & F_{33}(t,\delta\omega) & 0 & 0 & 0 & 0 \\
0 & 0 & E_{22}(t) & 0 & 00000 & 0 & 0 & 0 & F_{44}(t) & 0 & 0 & 0 \\
0 & 0 & 0 & E_{33}(t,\delta\omega) & 00000 & 0 & 0 & 0 & 0 & F_{55}(t,\delta\omega) & 0 & 0 \\
0 & 0 & 0 & 0 & 00000 & 0 & 0 & 0 & 0 & 0 & F_{66}(t,\delta\omega) & 0 \\
0 & 0 & 0 & 0 & 00000 & 0 & 0 & 0 & 0 & 0 & 0 & F_{77}(t,\delta\omega)
\end{pmatrix}$$

The elements of $U(t,\delta\omega)$ are listed in Table 3.4. Inspection of $U(t,\delta\omega)$ reveals that it only couples the irreducible operators $T_{1(0,\pm1)}$ with the irreducible operators $T_{3(0,\pm1)}$. Therefore, subsequent rotation and relaxation operations will never rotate or relax the spin-3/2 nuclei into states described by T_{00} or T_{2m}. It is sufficient to use only the

ten T_{1m} and T_{3m} irreducible operators when describing the dynamics of quadrupole relaxed spin-3/2 nuclei.

TABLE 3.4

Elements of Evolution Matrix $U_{ij}(t, \delta\omega)$

Matrix Elements	Value
$C^*_{11}(t,\delta\omega)$,$C_{33}(t,\delta\omega)$	$e^{i\delta\omega t}(\frac{3}{5}e^{-t/T_{2f}} + \frac{2}{5}e^{-t/T_{2s}})$
$C_{22}(t)$	$\frac{1}{5}e^{-t/T_{1f}} + \frac{4}{5}e^{-t/T_{1s}}$
$D_{11}(t,\delta\omega)$,$E_{11}(t,\delta\omega)$,$D^*_{33}(t,\delta\omega)$,$E^*_{33}(t,\delta\omega)$	$e^{i\delta\omega t}\frac{\sqrt{6}}{5}(e^{-t/T_{2f}} - e^{-t/T_{2s}})$
$D_{22}(t)$,$E_{22}(t)$	$\frac{2}{5}(e^{-t/T_{1f}} - e^{-t/T_{1s}})$
$F_{11}(t,\delta\omega)$,$F^*_{77}(t,\delta\omega)$	$e^{i3\delta\omega t}e^{-t/T_{23}}$
$F_{22}(t,\delta\omega)$,$F^*_{66}(t,\delta\omega)$	$e^{i2\delta\omega t}e^{-t/T_{22}}$
$F_{33}(t,\delta\omega)$,$F^*_{55}(t,\delta\omega)$	$e^{i\delta\omega t}(\frac{2}{5}e^{-t/T_{2f}} + \frac{3}{5}e^{-t/T_{2s}})$
$F_{44}(t)$	$\frac{4}{5}e^{-t/T_{1f}} + \frac{1}{5}e^{-t/T_{1s}}$

The relaxation times T_{1s} and T_{1f} characterize the relaxation of the Z-magnetization. The relaxation times T_{2s} and T_{2f} characterize the relaxation of the transverse magnetization. The relaxation times T_{22} and T_{23} respectively characterize the relaxation of the 2Q and 3Q coherences. The resonance offset is $\delta\omega$. The asterisks in Table 3.3 and Table 3.4 denote complex conjugation.

3.4 Calculations

3.4.1 Steady State for GS3Q Filter

The evolution of the density operator ρ caused by the application of the modified GS3Q filter described in Section 2.4 may be written

$$\rho_M^{GS3Q}(\tau_s, \delta\omega_1, \delta\omega_2, \omega_{off}) = \tag{3.10}$$

$$M_8(\tau_s,\delta\omega_1,\delta\omega_2)[M_7(\delta\omega_1)[M_6[M_5[M_4(\tau_s,\delta\omega_1,\delta\omega_2)[M_3(\delta\omega_1)[M_2 \times [M_1\rho_{eq}+G(\frac{\tau_1}{2})]+G(\frac{\tau_1}{2})]+G(\tau_2)]+G(\tau_{rg}+\tau_s+\tau_{cg})] + G(\frac{\tau_1}{2})]+G(\frac{\tau_1}{2})]+G(\tau_2)]+G(\tau_{rg}+\tau_s+\tau_{cg}), \tag{3.11}$$

where the M operators for the modified GS3Q filter are

$$M_1 = U(\frac{\tau_1}{2},\omega_{off})R(\frac{\pi}{2},0), \tag{3.12}$$

$$M_2 = U(\frac{\tau_1}{2},\omega_{off})R(\pi,\frac{\pi}{2}), \tag{3.13}$$

$$M_3(\delta\omega_1) = U(\tau_2,\omega_{off}+\delta\omega_1)R(\frac{\pi}{2},\frac{\pi}{2}), \tag{3.14}$$

$$M_4(\tau_s,\delta\omega_1,\delta\omega_2) = U(\tau_{cg},\omega_{off}+\delta\omega_2)U(\tau_s,\omega_{off})U(\tau_{rg},\omega_{off}+\delta\omega_1)R(\frac{\pi}{2},\frac{\pi}{2}), \tag{3.15}$$

$$M_5 = U(\frac{\tau_1}{2},\omega_{off})R(\frac{\pi}{2},\pi), \tag{3.16}$$

$$M_6 = U(\frac{\tau_1}{2},\omega_{off})R(\pi,-\frac{\pi}{2}), \tag{3.17}$$

$$M_7(\delta\omega_1) = U(\tau_2,\omega_{off}+\delta\omega_1)R(\frac{\pi}{2},-\frac{\pi}{2}), \tag{3.18}$$

$$M_8(\tau_s,\delta\omega_1,\delta\omega_2) = U(\tau_{cg},\omega_{off}+\delta\omega_2)U(\tau_s,\omega_{off})U(\tau_{rg},\omega_{off}+\delta\omega_1)R(\frac{\pi}{2},\frac{\pi}{2}). \tag{3.19}$$

The $\delta\omega_1$ term is included to describe off-resonance precession due to the G_{3Q} gradient. The $\delta\omega_2$ term is included to describe off-resonance precession due to the crusher gradient. The ω_{off} term is included to describe off-resonance precession due to inhomogeneities in the static magnetic field.

The conventional GS3Q filter does not contain a crusher gradient or two-step phase cycling. The N operators for the conventional GS3Q filter are listed below,

$$N_1 = U(\frac{\tau_1}{2},\omega_{off})R(\frac{\pi}{2},0), \tag{3.20}$$

$$N_2 = U(\frac{\tau_1}{2},\omega_{off})R(\pi,\frac{\pi}{2}), \tag{3.21}$$

$$N_3(\delta\omega_1) = U(\tau_2,\omega_{off}+\delta\omega_1)R(\frac{\pi}{2},\frac{\pi}{2}), \tag{3.22}$$

$$N_4(\tau_s,\delta\omega_1,\delta\omega_2) = U(\tau_{cg},\omega_{off})U(\tau_s,\omega_{off})U(\tau_{rg},\omega_{off}+\delta\omega_1)R(\frac{\pi}{2},\frac{\pi}{2}), \tag{3.23}$$

$$N_5 = U(\frac{\tau_1}{2},\omega_{off})R(\frac{\pi}{2},\pi), \tag{3.24}$$

$$N_6 = U(\frac{\tau_1}{2},\omega_{off})R(\pi,-\frac{\pi}{2}), \tag{3.25}$$

$$N_7(\delta\omega_1) = U(\tau_2,\omega_{off}+\delta\omega_1)R(\frac{\pi}{2},-\frac{\pi}{2}), \tag{3.26}$$

$$N_8(\tau_s,\delta\omega_1,\delta\omega_2) = U(\tau_{cg},\omega_{off}+\delta\omega_2)U(\tau_s,\omega_{off})U(\tau_{rg},\omega_{off}+\delta\omega_1)R(\frac{\pi}{2},-\frac{\pi}{2}). \tag{3.27}$$

Substituting these N operators for the M operators yields ρ_N^{GS3Q} for the conventional GS3Q filter.

At sufficiently short repetition times the spins will not re-establish thermal equilibrium between subsequent applications of the GS3Q filter. Not all of the coherences will have decayed away before the next application of the subsequent filter. After sufficient number of applications of the filter, the magnitude of the residual coherence at the beginning of the next GS3Q filter reaches a steady state. The steady state density operator ρ_{ss} is found by setting $\rho(t)$ equal to $\rho(0)$ in the evolution equation and solving for $\rho_M^{ss}(\tau_s,\delta\omega_1,\delta\omega_2,\omega_{off})$,

$$\begin{aligned}\rho_M^{ss}(\tau_s,\delta\omega_1,\delta\omega_2,\omega_{off}) = \\ [I - M_8(\tau_s,\delta\omega_1,\delta\omega_2)M_7(\delta\omega_1)M_6M_5M_4(\tau_s,\delta\omega_1,\delta\omega_2)M_3(\delta\omega_1)M_2M_1]^{-1} \\ \times (M_8(\tau_s,\delta\omega_1,\delta\omega_2)[M_7(\delta\omega_1)[M_6[M_5[M_4(\tau_s,\delta\omega_1,\delta\omega_2)[M_3(\delta\omega_1) \\ \times [M_2G(\frac{\tau_1}{2}) + G(\frac{\tau_1}{2})] + G(\tau_2)] + G(\tau_{rg}+\tau_s+\tau_{cg})] \\ + G(\frac{\tau_1}{2})] + G(\frac{\tau_1}{2})] + G(\tau_2)] + G(\tau_{rg}+\tau_s+\tau_{cg})) .\end{aligned} \tag{3.28}$$

(3.29)

Substituting the N operators for the M operators gives ρ_N^{ss} for the conventional GS3Q filter.

3.4.2 3Q Signal to Noise Ratio

The density operator following the first G_{3Q} refocusing gradient is

$$\rho_M^a(\tau_s,\delta\omega_1,\delta\omega_2,\omega_{off})=M_4^a(\delta\omega_1)[M_3(\delta\omega_1)[M_2[M_1\rho_M^{ss}(\tau_s,\delta\omega_1,\delta\omega_2,\omega_{off})$$

$$+ G(\frac{\tau_1}{2})] + G(\frac{\tau_1}{2})] + G(\tau_2)] + G(\tau_{rg}), \tag{3.30}$$

where $M_4^a(\delta\omega_1) = U(\tau_{rg}, \omega_{off} + \delta\omega_1)R(\frac{\pi}{2}, \frac{\pi}{2})$. The density operator following the second 3Q refocusing gradient is

$$\rho_M^b(\tau_s, \delta\omega_1, \delta\omega_2, \omega_{off}) = M_8^b(\delta\omega_1)[M_7(\delta\omega_1)[M_6[M_5[M_4^b(\tau_s, \delta\omega_2)\rho_M^a(\tau_s, \delta\omega_1, \delta\omega_2, \omega_{off}) + G(\tau_s + \tau_{cg})] + G(\frac{\tau_1}{2})] + G(\frac{\tau_1}{2})] + G(\tau_2)] + G(\tau_{rg}), \tag{3.31}$$

where $M_8^b(\delta\omega_1) = U(\tau_{rg}, \omega_{off}+\delta\omega_1)R(\frac{\pi}{2}, \frac{\pi}{2})$ and $M_4^b(\tau_s, \delta\omega_2) = U(\tau_{rg}, \omega_{off}+\delta\omega_2)U(\tau_s, \omega_{off})$. Taking the difference of $\rho_M^a(\tau_s, \delta\omega_1, \delta\omega_2, \omega_{off})$ and $\rho_M^b(\tau_s, \delta\omega_1, \delta\omega_2, \omega_{off})$ and summing over spins with resonance offsets $\delta\omega_1$ and $\delta\omega_2$ each ranging from 0 to 2π yields

$$\Delta\rho_M(\tau_s, \omega_{off}) = \sum_{\delta\omega_1}\sum_{\delta\omega_2}\left(\rho_M^a(\tau_s, \delta\omega_1, \delta\omega_2, \omega_{off}) - \rho_M^b(\tau_s, \delta\omega_1, \delta\omega_2, \omega_{off})\right). \tag{3.32}$$

Using the (31) and (3(-1)) elements of $\Delta\rho_M(\tau_s, \omega_{off})$, the 3Q signal from the modified GS3Q filter is

$$S_M^{3Q}(t, \tau_s, \omega_{off}) = D'_{11}(t, 0)\frac{\rho_M^{3Q}(\tau_s, \omega_{off})}{D'_{11}(\tau_{rg}, 0)}, \tag{3.33}$$

where $\rho_M^{3Q}(\tau_s, \omega_{off}) = \frac{1}{\sqrt{2}}|\Delta\rho_{M(31)}(\tau_s, \omega_{off}) - \Delta\rho_{M(3(-1))}(\tau_s, \omega_{off})|$ and $D'_{11}(t, 0) = \frac{\sqrt{6}}{5}(e^{-t/T'_{2f}} - e^{-t/T'_{2s}})$. The form of $\rho_M^{3Q}(\tau_s, \omega_{off})$ reflects that only one component of the transverse magnetization was detected since our RF coil was not used in quadrature. The transverse relaxation times T'_{2s} and T'_{2f} include the effects of inhomogeneities in the static field. The time origins for $D'_{11}(t, 0)$ immediately follow the fourth and eighth RF pulses. The signal is sampled from τ_{rg} to $\tau_{rg} + \tau_s$. $D'_{11}(t, 0)$ is evaluated on resonance in this calculation since we are only concerned with the magnitude of the modified GS3Q filtered signal.

The amplitude of the 3Q spectral line apodized with $D'_{11}(t, 0)$ is

$$A_M^{3Q} = \frac{\rho_M^{3Q}(\tau_s, \omega_{off})}{D'_{11}(\tau_{rg}, 0)}\int_{\tau_{rg}}^{(\tau_{rg}+\tau_s)} |D'_{11}(t, 0)|^2 dt. \tag{3.34}$$

The standard deviation of the apodized noise is

$$\sigma_a = \sigma\sqrt{\int_{\tau_{rg}}^{(\tau_{rg}+\tau_s)} |D'_{11}(t, 0)|^2 dt}, \tag{3.35}$$

where σ is the standard deviation of the noise. The ratio of A_M^{3Q} and σ_a give the apodized 3Q filtered signal to noise ratio obtained in a fixed time T_{exp},

$$\mathrm{SNR}_M^{3Q} = \sqrt{\frac{T_{exp}}{T_R}} \frac{\rho_M^{3Q}(\tau_s, \omega_{off})}{\sigma D'_{11}(\tau_{rg}, 0)} \sqrt{\int_{\tau_{rg}}^{(\tau_{rg}+\tau_s)} |D'_{11}(t,0)|^2 dt}. \tag{3.36}$$

The term $\sqrt{T_{exp}/T_R}$ increases the SNR_M^{3Q} due to the averaging of a number of shots [28]. Repeating this calculation with the N operators instead of the M operators yields SNR_N^{3Q} for the conventional GS3Q filter.

3.4.3 Suppression Factor and Spurious 1Q Ratio

The suppression of 1Q signals is calculated by dividing the spurious 1Q signal from the modified and conventional GS3Q filtered experiment by the 1Q signal from a one pulse experiment. The spurious contribution of 1Q coherences to the modified GS3Q filtered signal is determined by calculating $\Delta\rho_M(\tau_s, \omega_{off})$ with the operators $M_4^{1Q}(\tau_s, \delta\omega_1, \delta\omega_2, \omega_{off})$ and $M_8^{1Q}(\tau_s, \delta\omega_1, \delta\omega_2, \omega_{off})$ instead of with $M_4^a(\tau_s, \delta\omega_1, \delta\omega_2, \omega_{off})$ and $M_8^b(\tau_s, \delta\omega_1, \delta\omega_2, \omega_{off})$. The operators $M_4^{1Q}(\tau_s, \delta\omega_1, \delta\omega_2, \omega_{off})$ and $M_8^{1Q}(\tau_s, \delta\omega_1, \delta\omega_2, \omega_{off})$ use rotation matrices $R(\frac{\pi}{2}, \frac{\pi}{2})$ and $R(\frac{\pi}{2}, -\frac{\pi}{2})$ in which the elements B_{31}, B_{37},B_{51}, and B_{57} are replaced by zero. Using the (11) and (1(-1)) elements of $\Delta\rho_M^{1Q}(\tau_s, \omega_{off})$ the spurious 1Q signal from the modified GS3Q filtered experiment is

$$S_M^{1Q}(t, \tau_s, \omega_{off}) = C'_{11}(t,0) \frac{\rho_M^{1Q}(\tau_s, \omega_{off})}{C'_{11}(\tau_{rg}, 0)}, \tag{3.37}$$

where $\rho_M^{1Q}(\tau_s, \omega_{off}) = \frac{1}{\sqrt{2}} |\Delta\rho_{M(11)}^{1Q}(\tau_s, \omega_{off}) - \Delta\rho_{M(1(-1))}^{1Q}(\tau_s, \omega_{off})|$. The amplitude of the apodized spurious 1Q spectral line from the modified GS3Q filtered experiment is

$$A_M^{1Q} = \frac{\rho_{1Q}^{GS3Q}(\tau_s, \omega_{off})}{C'_{11}(\tau_{rg}, 0)} \int_{\tau_{rg}}^{(\tau_{rg}+\tau_s)} C'_{11}(t,0) D'_{11}(t,0) dt, \tag{3.38}$$

where the apodizing function $D'_{11}(t,0)$ is used.

We designed the one pulse experiment by setting the amplitude of the G_{3Q}

gradient to zero and by setting the flip angle of the first, second, third, fifth, sixth, and seventh pulses to zero. The steady state density operator $\rho_O^{ss}(\tau_s, \omega_{off})$ is obtained by replacing the M operators with the O operators:

$$O_1 = U(\frac{\tau_1}{2}, \omega_{off})R(0,0), \tag{3.39}$$

$$O_2 = U(\frac{\tau_1}{2}, \omega_{off})R(0,0), \tag{3.40}$$

$$O_3 = U(\tau_2, \omega_{off})R(0,0), \tag{3.41}$$

$$O_4(\tau_s, \delta\omega_2) = U(\tau_{cg}, \omega_{off} + \delta\omega_2)U(\tau_s, \omega_{off})U(\tau_{rg}, \omega_{off})R(\frac{\pi}{2}, \frac{\pi}{2}), \tag{3.42}$$

$$O_5 = U(\frac{\tau_1}{2}, \omega_{off})R(0,0), \tag{3.43}$$

$$O_6 = U(\frac{\tau_1}{2}, \omega_{off})R(0,0), \tag{3.44}$$

$$O_7 = U(\tau_2, \omega_{off})R(0,0), \tag{3.45}$$

$$O_8(\tau_s, \delta\omega_2) = U(\tau_{cg}, \omega_{off} + \delta\omega_2)U(\tau_s, \omega_{off})U(\tau_{rg}, \omega_{off})R(\frac{\pi}{2}, -\frac{\pi}{2}). \tag{3.46}$$

The density operator $\Delta\rho_O(\tau_s, \omega_{off})$ is calculated identically to $\Delta\rho_M(\tau_s, \omega_{off})$, except that the O operators are used in place of the T operators. Using the (11) and (1(-1)) elements of $\Delta\rho_O(\tau_s, \omega_{off})$ the 1Q signal from the one pulse experiment is

$$S_O^{1Q}(t, \tau_s, \omega_{off}) = C'_{11}(t,0)\frac{\rho_O^{1Q}(\tau_s, \omega_{off})}{C'_{11}(\tau_{rg}, 0)}, \tag{3.47}$$

where $\rho_O^{1Q}(\tau_s, \omega_{off}) = \frac{1}{\sqrt{2}}|\Delta\rho_{O(11)}(\tau_s, \omega_{off}) - \Delta\rho_{O(1(-1))}(\tau_s, \omega_{off})|$ and $C'_{11}(t,0) = \frac{3}{5}e^{-t/T'_{2f}} + \frac{2}{5}e^{-t/T'_{2s}}$. The amplitude of an apodized 1Q spectral line from the one pulse experiment is

$$A_O^{1Q} = \frac{\rho_O^{1Q}(\tau_s, \omega_{off})}{C'_{11}(\tau_{rg}, 0)} \int_{\tau_{rg}}^{(\tau_{rg}+\tau_s)} C'_{11}(t,0)D'_{11}(t,0)dt, \tag{3.48}$$

where the apodizing function $D'_{11}(t,0)$ is used.

The suppression factor is defined to be

$$\text{Suppression Factor} = \frac{A_M^{1Q}}{A_O^{1Q}}. \tag{3.49}$$

The ratio of spurious 1Q signal from a modified GS3Q filtered experiment divided by the 3Q signal from a modified GS3Q filtered experiment is referred to as the spurious 1Q ratio,

$$\text{Spurious 1Q Ratio} = \frac{A_M^{1Q}}{A_M^{3Q}}. \tag{3.50}$$

Chapter 4

Experiments Using GS3Q Filter

Repetition times reported in the literature for ^{23}Na multiple-quantum filters typically range from 200 to 300 ms [3, 7, 8, 21], although recently an experiment with a 105 ms repetition time was reported [9]. In this chapter it is shown that the repetition time of 55 ms maximizes the SNR_{3Q} calculated in Section 3.4 for GS3Q filtered experiments using ^{23}Na in a 4% agarose gel. The relaxation times for ^{23}Na in the 4% agarose gel were found to be similar to relaxation times for physiological ^{23}Na [3]. It is also shown that significant spurious 1Q signal results in conventional GS3Q filtered experiments for repetition times below 100 ms. Measurements and calculations are presented which show that the spurious 1Q signal from modified GS3Q filtered experiments is substantially reduced compared to the conventional GS3Q filtered experiments. In Section 4.1, the six measured relaxation times for ^{23}Na in a 4% agarose gel are presented. In Section 4.2, the methods used in the measurements and calculations of SNR_{3Q}, suppression factor, and spurious 1Q ratio are discussed. In Section 4.3, the results from the measurements and calculations are presented.

4.1 Measurements of ^{23}Na relaxation times

As discussed Chapter 2, there are six relaxation times for BER ^{23}Na, T_{1f}, T_{1s}, T_{2f}, T_{2s}, T_{22}, T_{23} and two for SER ^{23}Na T_1 and T_2. It is necessary to know all six relaxation times for the BER ^{23}Na in order to calculate the SNR_{3Q}, suppression factor, and the spurious 1Q ratio for the GS3Q filters. One approach of obtaining T_{2f} and T_{2s} is to fit the sum of the biexponential function $C_{11}(t, \delta\omega)$ from Table 3.4 and the single-exponential function e^{-t/T_2} to the ^{23}Na signal measured from a conventional one pulse experiment. This approach is difficult to implement *in vivo* due to the large SER ^{23}Na signal. This method for measuring relaxation times is also limited since it cannot be used to measure T_{1f}, T_{1s}, T_{22}, and T_{23}. Relaxation measurement techniques which utilize MQ filters overcome these difficulties.

The most accurate way to measure *in vivo* T_{2f}, T_{2s} is with a refocused two-dimensional multiple-quantum filtering approach [5], see Figure 4.1. The advantage of this method is that NMR signal is obtained from only BER ^{23}Na. All of the SER ^{23}Na signal is suppressed. During the preparation portion of this sequence, the anti-phase coherence evolves as $D_{11}(t, 0)$.

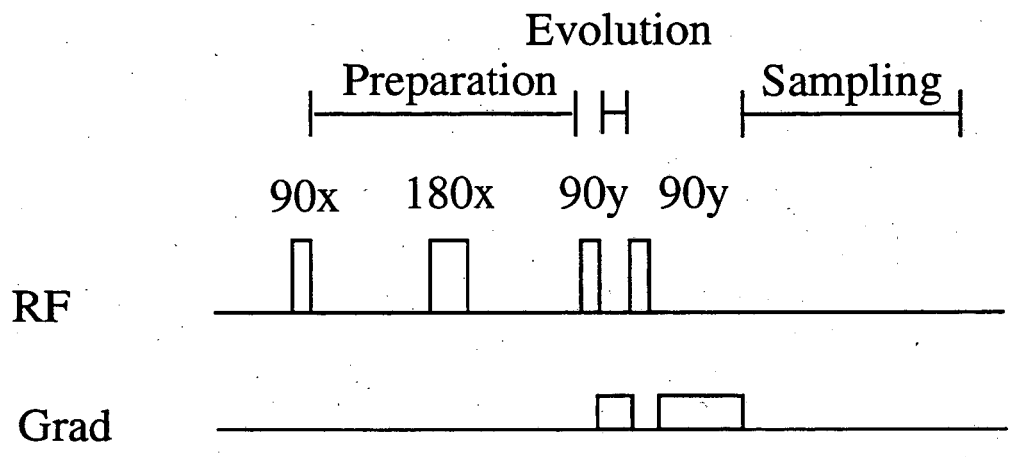

Figure 4.1: GS3Q sequence used to measure T_{2f},T_{2s}, and T'_{23}.

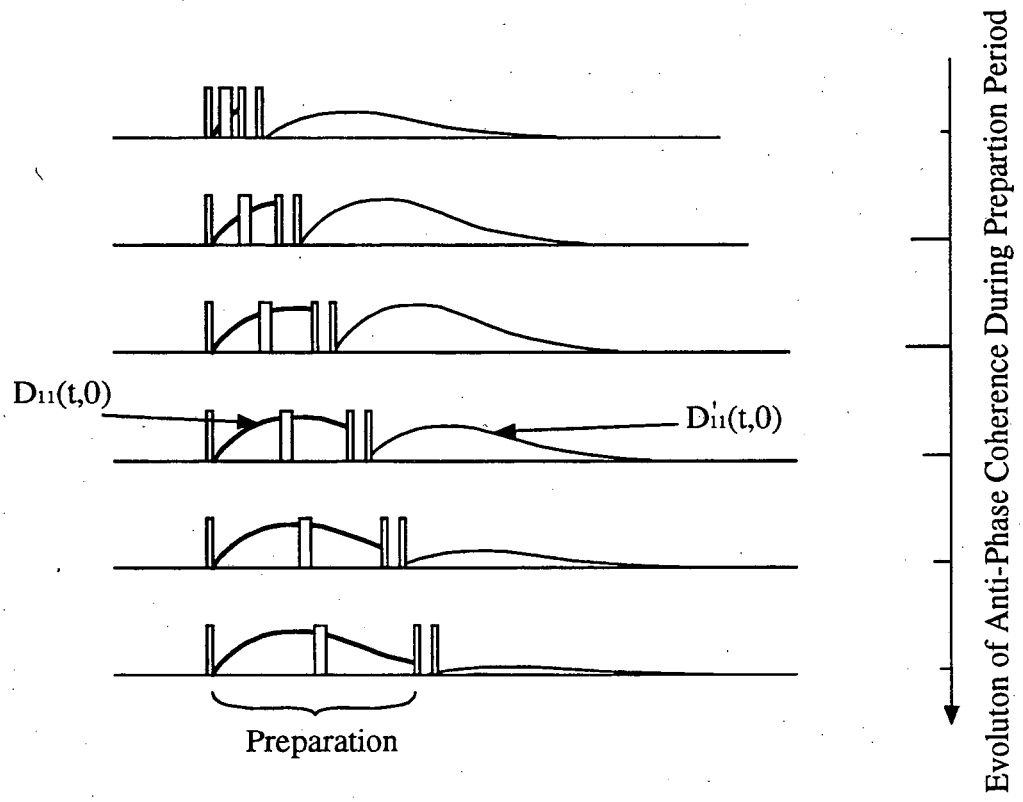

Figure 4.2: Two-dimensional multiple-quantum approach for sampling evolution of anti-phase coherence during preparation time. The definitions of $D_{11}(t,0)$ and $D'_{11}(t,0)$ are given in the text.

By performing repeated experiments with different preparation times, it is possible to measure the evolution of the anti-phase coherence term during the preparation period, see Figure 4.2. The measured evolution of the anti-phase coherence during the preparation period may be fitted to the function $D_{11}(t,0)$ from Section 3.3 to get T_{2f} and T_{2s}. Using a similar approach as just described, but incrementing the evolution time instead of the preparation time, gives an accurate measurement of T'_{23}. During the sampling portion of this sequence, the unrefocused signal evolves as $D'_{11}(t,0) = \frac{\sqrt{6}}{5}(e^{-t/T'_{2f}} - e^{-t/T'_{2s}})$. The primed relaxation times include the effects of static field inhomogeneity.

To measure the short T'_{22} relaxation time, it is better to use a phase-cycled 2Q

filter instead of the gradient-selected 2Q filter. The advantage of the phase-cycled 2Q filter is that the evolution period can be as short as ten microseconds, while the gradient-selected 2Q filter requires at least one millisecond for the evolution time. The short evolution time of the phase-cycled 2Q filter provides more accurate measurements of the short T'_{22} term. The T'_{22} term is measured by performing repeated experiments in which the evolution period is incremented. A phase-cycled 3Q filter was not necessary for the T'_{23} term since the T'_{23} relaxation time is substantially longer than the T'_{22} relaxation time. T_{22} and T_{23} were obtained from T'_{22} and T'_{23} using the measured inhomogeneity of the static magnetic field. The signal acquired during the sampling period of a single experiment may be fitted to the function $D'_{11}(t,0)$ to get T'_{2f} and T'_{2s}.

Accurate measurements of T_{1s} and T_{1f} term are difficult to obtain since T_{1s} and T_{1f} are relatively similar. The pulse sequence used to measure these terms is shown in Figure 4.3 [23].

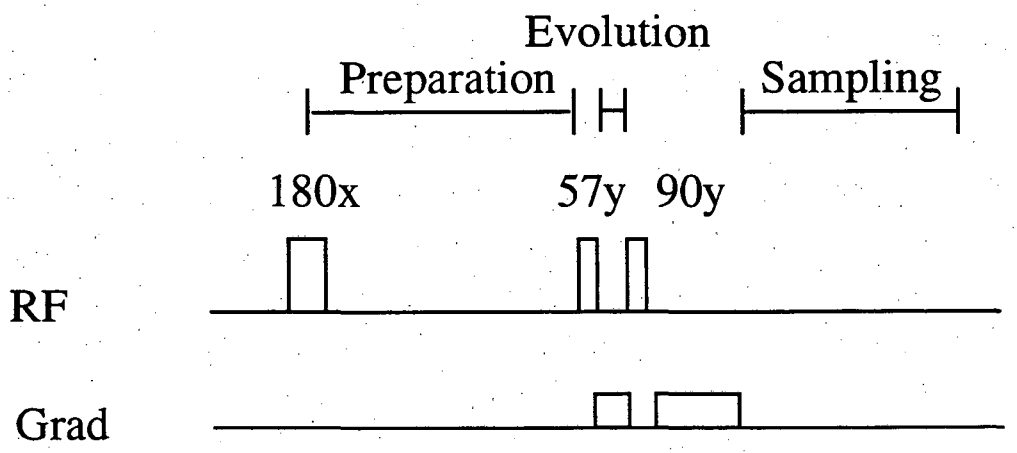

Figure 4.3: Gradient-selected triple-quantum sequence used to measure T_{1s} and T_{1f}.

The 57 degree flip angle for the second pulse optimizes the production of 3Q coherence in the evolution period. Using the 2-dimensional approach of incrementing the preparation time with repeated experiments gives a measurement of the population relaxation term, $\frac{2}{5}(e^{-t/T_{1f}} - e^{-t/T_{1s}})$. Fitting this expression to the experimental data

yields measurements for T_{1s} and T_{1f}.

The measured relaxation parameters of ^{23}Na in the 2.0 M NaCl, 4% agarose phantom are displayed in Table 4.1. The measured relaxation parameters of the ^{23}Na in the 2.0 M aqueous phantom were T_1=50.0 $\pm$ 2.0 ms, T_2=49.0 $\pm$ 2.0 ms, and T_2'=32.0 $\pm$ 1.0 ms. The increase in measurement error of the unprimed versus the primed relaxation times is due to limits of accuracy in measuring the contribution of static magnetic field inhomogeneities to the relaxation times.

TABLE 4.1

Measured Relaxation Parameters of 2.0 M NaCl + 4% Agarose Phantom

Parameter	Value (ms)
T_{1s}	24.6 $\pm$ 2.0
T_{1f}	16.6 $\pm$ 2.0
T_{2s}	22 $\pm$ 3
T_{2f}	3.6 $\pm$ 0.2
T_{22}	3.6 $\pm$ 0.2
T_{23}	24 $\pm$ 8
T_{2s}'	19 $\pm$ 1
T_{2f}'	3.5 $\pm$ 0.1
T_{22}'	3.4 $\pm$ 0.
T_{23}'	17 $\pm$ 1

4.2 Methods

The SNR of the GS3Q filters were measured using two sets of experiments. In the first set of experiments the conventional and modified GS3Q filtered ^{23}Na signals

from the gel and aqueous phantoms were measured for different T_R and resonance offset. In the second set of experiments the noise was measured for different T_R by shifting the frequency of the RF by 20 kHz. The quality factor of our RF coil was 200, so the 20 kHz shift in the RF frequency reduced the efficiency of the RF coil by approximately 5%. These experimental data were apodized with the function $D'_{11}(t,0)$. Using the measured ^{23}Na relaxation rates in Table 4.1, the SNR_{3Q} from Section 3.4 was calculated for various T_R and resonance offsets and compared with the measured modified and conventional GS3Q filtered SNR.

Sodium in an aqueous NaCl solution does not give a 3Q signal, since the ^{23}Na ions are in the fast motional narrowing limit. Therefore any ^{23}Na signal detected from an aqueous NaCl solution using a GS3Q filter is spurious 1Q signal. The suppression factor was determined by dividing the spurious 1Q signal obtained from a GS3Q filtered experiment using the aqueous phantom by the 1Q signal obtained from a one pulse experiment using the same phantom. The suppression factor was measured for various T_R. These experimental data were apodized with the function $D'_{11}(t,0)$. Using the measured ^{23}Na relaxation parameters of the aqueous phantom the suppression factor from the Section 3.4 was calculated for various T_R and compared to the measured suppression factors.

The spurious 1Q ratio defined in the Section 3.4 was also calculated and compared to measurements. The ratio of the measured GS3Q filtered spurious 1Q signal from the aqueous phantom and the measured GS3Q filtered signal from the gel phantom were compared to the calculated spurious 1Q ratios for various T_R and resonance offsets. The experimental data were apodized with the function $D'_{11}(t,0)$.

The modified GS3Q filter parameters for the above experiments are listed in Table 4.2. The conventional GS3Q filter has the same parameters except that it lacks a crusher gradient and the RF phases are different (see Section 3.4). A 13 cm diameter and 16 cm long birdcage RF coil and a 40 cm bore 2.35 Tesla Bruker magnet were used. The RF coil was not driven in quadrature. The gradient amplitudes were chosen to yield adequate dephasing across the sample without inducing excessive eddy currents. Thirteen different repetition times were used for the experiments. The repetition times were changed with τ_s by taking different numbers of sample points.

The sampling interval was 100 μs, thus T_R = 18.75 ms + 100 μs $\times$ (number sample points). The number of sample points ranged from 128 to 2800 points yielding repetition times of 32 to 300 ms. Frequency offsets were obtained by shifting the frequency of the RF pulses. The total time of each experiment was T_{exp} = 7 s. To insure that the spins were in steady state, the modified GS3Q filter was run for a 7 s preparation period before the experiment during which no sampling occurred.

Calculations using the analysis presented in the Chapter 3 were performed using Mathematica (Wolfram Research, Inc.) on a IBM RS6000 workstation. A homogeneous two-dimensional group of 625 (25 x 25) spins was used in the calculation. For all of the theoretical calculations a single factor was used to scale the calculated results to match the amount of ^{23}Na and the RF coil sensitivity in the experiments.

TABLE 4.2

Modified Gradient-Selected Triple-Quantum Filter Parameters

Parameter	Value
3Q Gradient Filter Amplitude	0.7 G/cm
Crusher Gradient Amplitude	0.3 G/cm
90° RF Pulse Duration	140 μs
180° RF Pulse Duration	280 μs
τ_1	$ln(T_{2f}/T_{2s})/((1/T_{2s}) - 1/T_{2f})$
τ_2	1 ms
τ_{rg}	3.0 ms
τ_{cg}	5.0 ms

4.3 Results

Figure 4.4 shows that SNR increases by a factor of two as T_R decreases from 300 ms to 55 ms for both the conventional and modified GS3Q filters. The improvement

in SNR with decreasing repetition time results from the averaging of signals [28]. Figure 4.5 shows that the suppression factor increases for decreasing T_R for both the conventional and modified GS3Q filter. Figure 4.5 also shows that the modified GS3Q filter suppresses spurious signals at short T_R better than the conventional filter. For T_R less than 70 ms the suppression factor increases more rapidly since saturation reduces the signal obtained from the one pulse experiment. For T_R larger than 120 ms the experimental suppression factor for the aqueous phantom was approximately 1/2500.

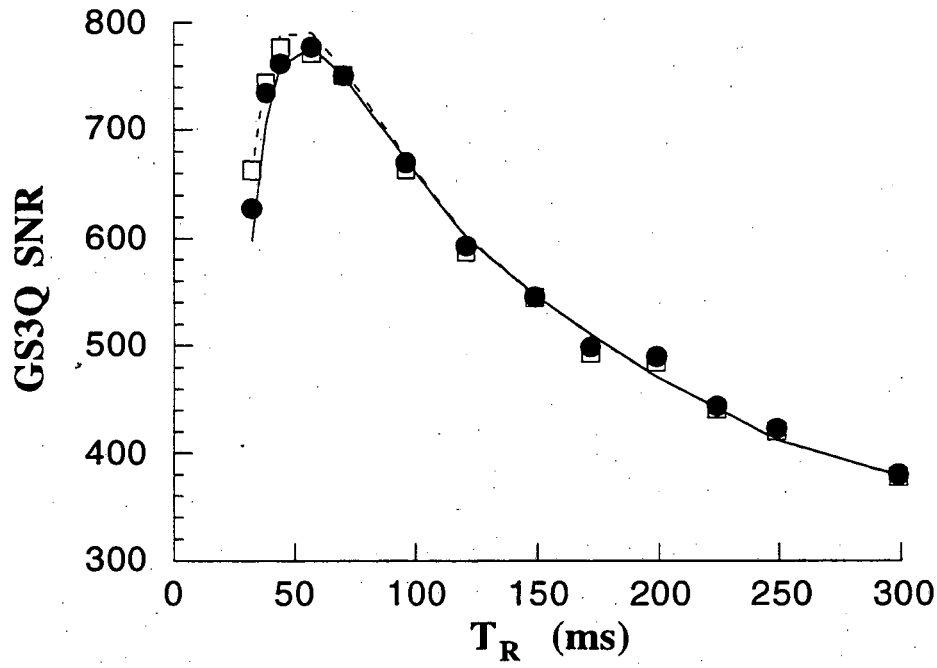

Figure 4.4: Triple-quantum filtered signal to noise ratio vs. repetition time for the modified gradient-selected triple-quantum filter. Open squares and closed circles are experimental points for conventional and modified GS3Q filters, respectively. Dashed and solid lines are theoretical predictions using the the SNR_{3Q} from Section 3.4 for conventional and modified GS3Q filters. The sample is a 4 cm diameter sphere containing 2.0 M NaCl and 4% agarose.

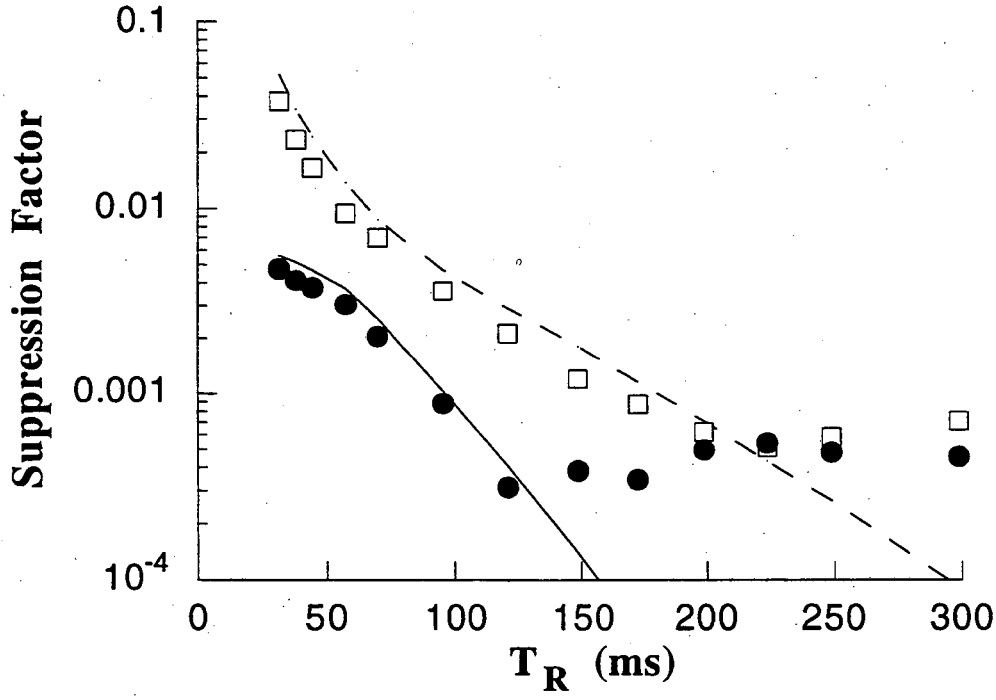

Figure 4.5: Plot of suppression factor versus repetition time. Open squares and closed circles are experimental points for conventional and modified GS3Q filters. Dashed and solid lines are theoretical predictions using the suppression factors in Section 3.4 for the conventional and modified GS3Q filters. The sample is a 4 cm diameter sphere containing 2.0 M NaCl in water.

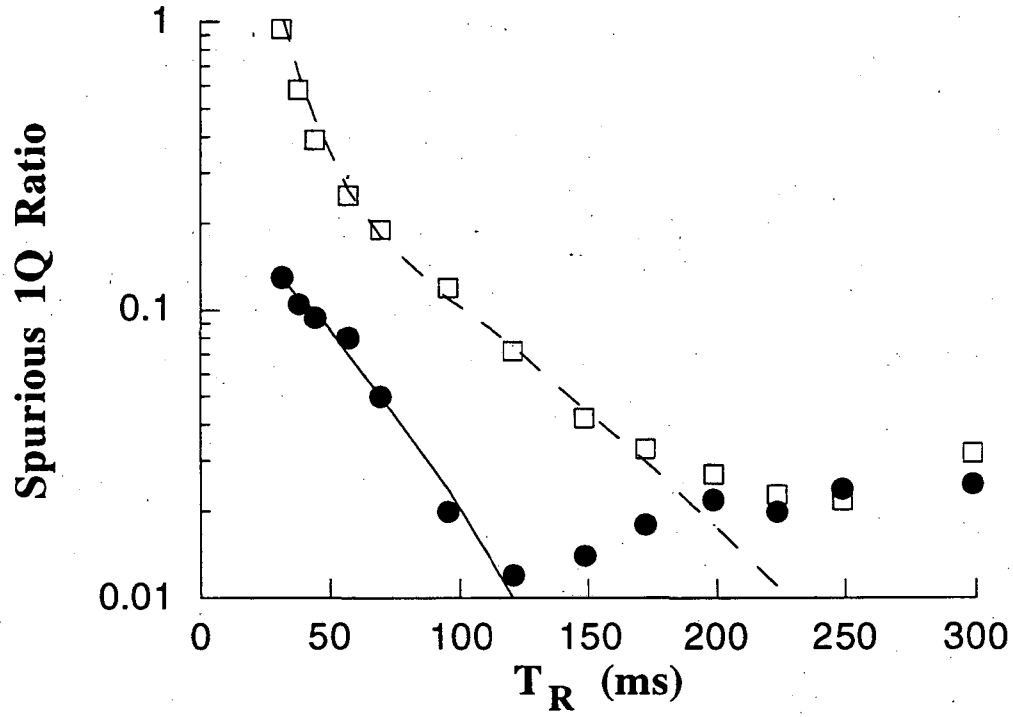

Figure 4.6: Plot of spurious one-quantum ratio versus repetition time. The solid circles are the experimental data points for the ratio of modified GS3Q filtered spurious 1Q signal from 2.0 M aqueous NaCl and modified GS3Q filtered signal from 2.0 M NaCl + 4% agarose. The open squares are the experimental data points using the conventional GS3Q filter. The solid line is the theoretical prediction, see Section 3.4, for spurious 1Q ratio of modified GS3Q filtered spurious 1Q signal from 2.0 M aqueous NaCl and modified GS3Q filtered 3Q signal from 2.0 M NaCl + 4% agarose. The dashed line is the theoretical prediction for the conventional GS3Q filter.

Figure 4.6 shows that the spurious 1Q ratio for the modified and conventional GS3Q filter with the aqueous phantom increases up to 0.12 and 1.0 as the T_R decreases to 32 ms. For T_R of 70 ms the spurious 1Q signal from the aqueous phantom is approximately 5% of the modified GS3Q filtered signal from the gel phantom.

Figure 4.7 shows the calculated and experimental measurements of SNR for the modified GS3Q filter plotted versus frequency offset. Figure 4.7 also shows the off-resonance dependence of the SNR from a modified GS3Q filter without the 180° refocusing pulses, an unrefocused GS3Q filter. The off-resonant frequency at which the non-refocused SNR reaches a minimum corresponds to the nuclear spins having precessed $\frac{(2n+1)\pi}{2}$ $(n = 0, 1, 2, ...)$ during the preparation period. As the preparation time is shortened, the off-resonant frequency of the first minimum grows larger. Recently an imaging sequence in which the phase encoding is performed during the preparation period was proposed [10]. The above results show that for unrefocused GS3Q filters with long preparation periods (>5 ms), significant loss of signal may occur due to off-resonant spins. In Figure 4.8 the spurious 1Q ratio is plotted versus frequency offset. Figure 4.8 shows that the spurious 1Q ratio does not increase for off-resonant spins.

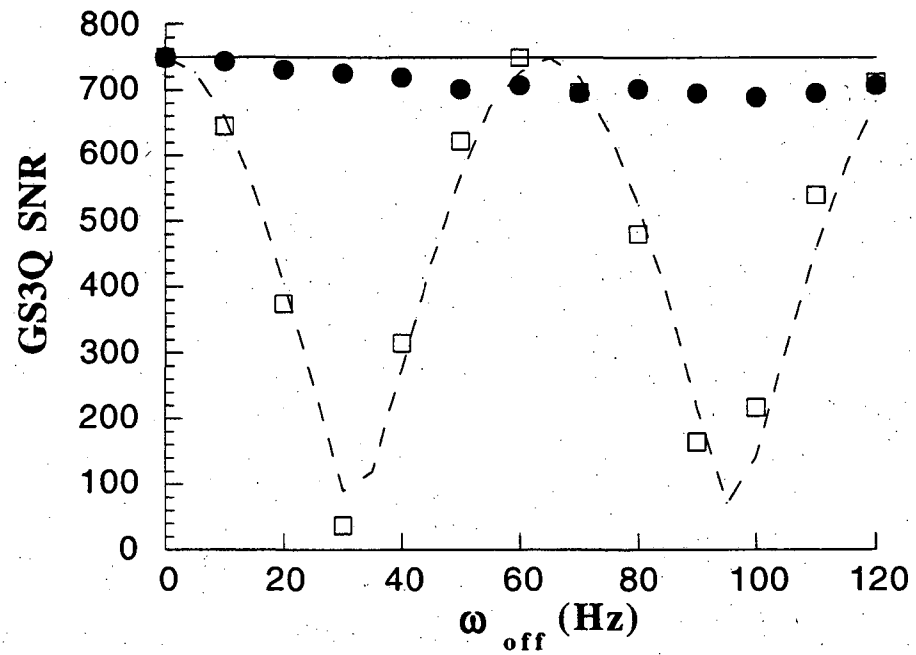

Figure 4.7: Triple-quantum filtered signal to noise ratio vs. resonance offset. The solid circles and open squares are the experimental points for the modified GS3Q filter with and without the 180° refocusing pulses. The solid line is the theoretical prediction of SNR_{3Q} from section 3.4 for the modified GS3Q filter. The dashed line is the theoretical prediction for the modified GS3Q filter without the 180° refocusing pulses. The sample is a 4 cm diameter sphere containing 2.0 M NaCl and 4% agarose. The repetition time is 70 ms. For this experiment 256 points were sampled at a rate of $1/(200\ \mu s)$. The 256 sampled points were zero-filled up to 2256 points.

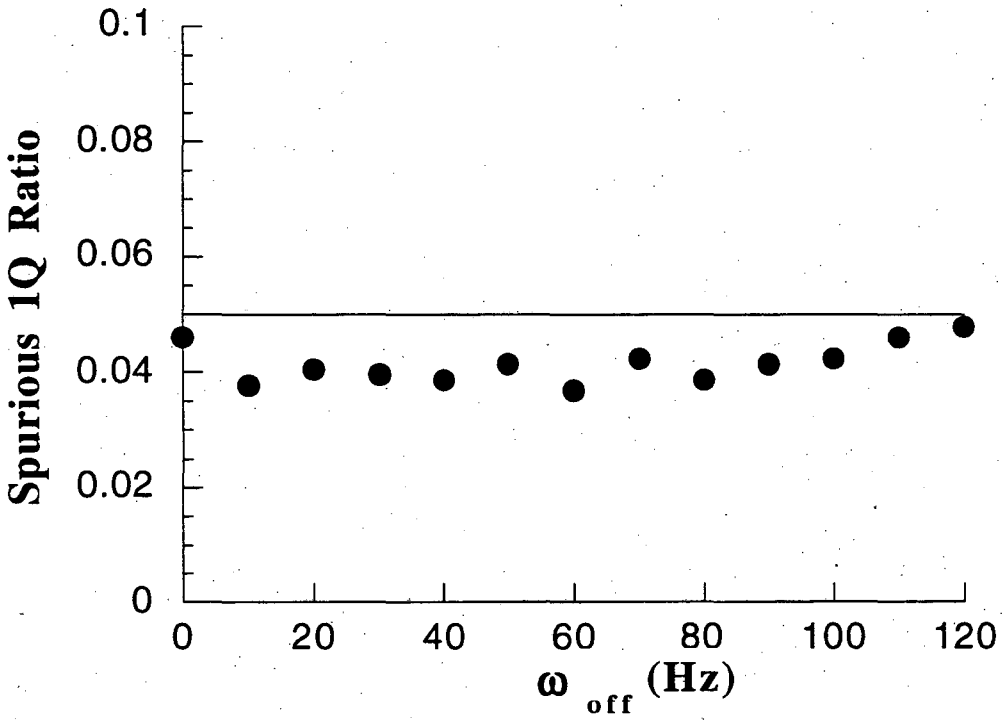

Figure 4.8: Spurious 1Q Ratio versus resonance offset. The solid circles are the experimental data points for the ratio of modified GS3Q filtered spurious 1Q from 2.0 M aqueous NaCl and modified GS3Q filtered signal from 2.0 M NaCl + 4% agarose. The solid line is the theoretical prediction, see Section 3.4, for the ratio of modified GS3Q filtered spurious 1Q signal from 2.0 M aqueous NaCl and modified GS3Q filtered 3Q signal from 2.0 M NaCl + 4% agarose. The samples are 4 cm diameter spheres. For this experiment 256 points were sampled at a rate of $1/(200\ \mu s)$. The 256 sampled points were zero-filled up to 2256 points. .

Chapter 5

MQ Imaging Experiments

In this chapter experiments using the modified GS3Q filter to image phantoms with physiological concentrations of BER ^{23}Na are presented. Using the results of these experiments it is concluded that GS3Q filtered imaging of BER ^{23}Na in the human brain should be possible. In Section 5.1, basic imaging principles emphasizing the usefulness of k-space are reviewed. In Section 5.2, the advantages and disadvantages of phase-cycled and gradient-selected approaches to multiple-quantum filtered imaging are examined. In Section 5.3, experiments using phase-cycled multiple-quantum filtered imaging of ^{23}Na phantoms at 4.7 Tesla are presented. In Section 5.4, experiments using modified gradient-selected triple-quantum filtered imaging of ^{23}Na phantoms at 2.35 Tesla are presented and the implications of the results are discussed.

5.1 Principles of NMR Imaging

Magnetic field gradients cause the nuclei in an NMR sample to precess at different frequency as a function of position in the sample. When the magnetic field gradient is removed, the phases of the nuclear spins are distributed in a helical fashion. The spatial frequency of the helical distribution is tighter for larger gradients or

longer duration gradients, see Figure 5.1.

The helical distribution of the phases of the nuclei acts like a filter selective for the spatial frequency of the helix. If the spatial distribution of the NMR sample is uniform, then the helical distribution of the spins will cause the NMR signal to cancel to zero. In contrast, if the spatial distribution of the sample is similar to the spatial frequency of the helical distribution of the spins, then the NMR signal will not cancel, see Figure 5.2.

A magnetic field gradient following a RF pulse and preceding the NMR sampling is referred to as a phase encode gradient [58], see Figure 5.3. The amplitude of the NMR signal following the phase encode gradient is the Fourier amplitude for the sample at the spatial frequency determined by the gradient. The sampled spatial frequency may be depicted with a k-space representation [59]. Performing repeated NMR experiments using phase encode gradients of different amplitude samples different points in k-space. The Fourier transform of the sampled k-space points produces an image of the NMR sample, see Figure 5.4.

An advantage of using phase encode gradients in NMR imaging is that the NMR signal at each k-space point is frequency encoded only with spectroscopic information. This fact is the basis for chemical-shift imaging. A disadvantage of using phase encode gradients for NMR imaging is that only one k-space point is collected with each FID. It often takes too long to collect a full k-space sampling using phase encode gradients. An additional problem with using phase encode gradients is sample movement. If the sample moves part way through sampling of k-space when using phase encode gradients, it is hard to correct the k-space sampling to account for the movement.

Another NMR imaging approach is to leave the gradient on during the sampling. This kind of gradient is called a read-out gradient [58], see Figure 5.5. When using a read-out gradient a dephasing gradient is applied after the RF pulse and before the sampling. During the sampling a read-out gradient is applied with opposite sign as the dephasing gradient. As time increases with the read-out gradient on, the spatial

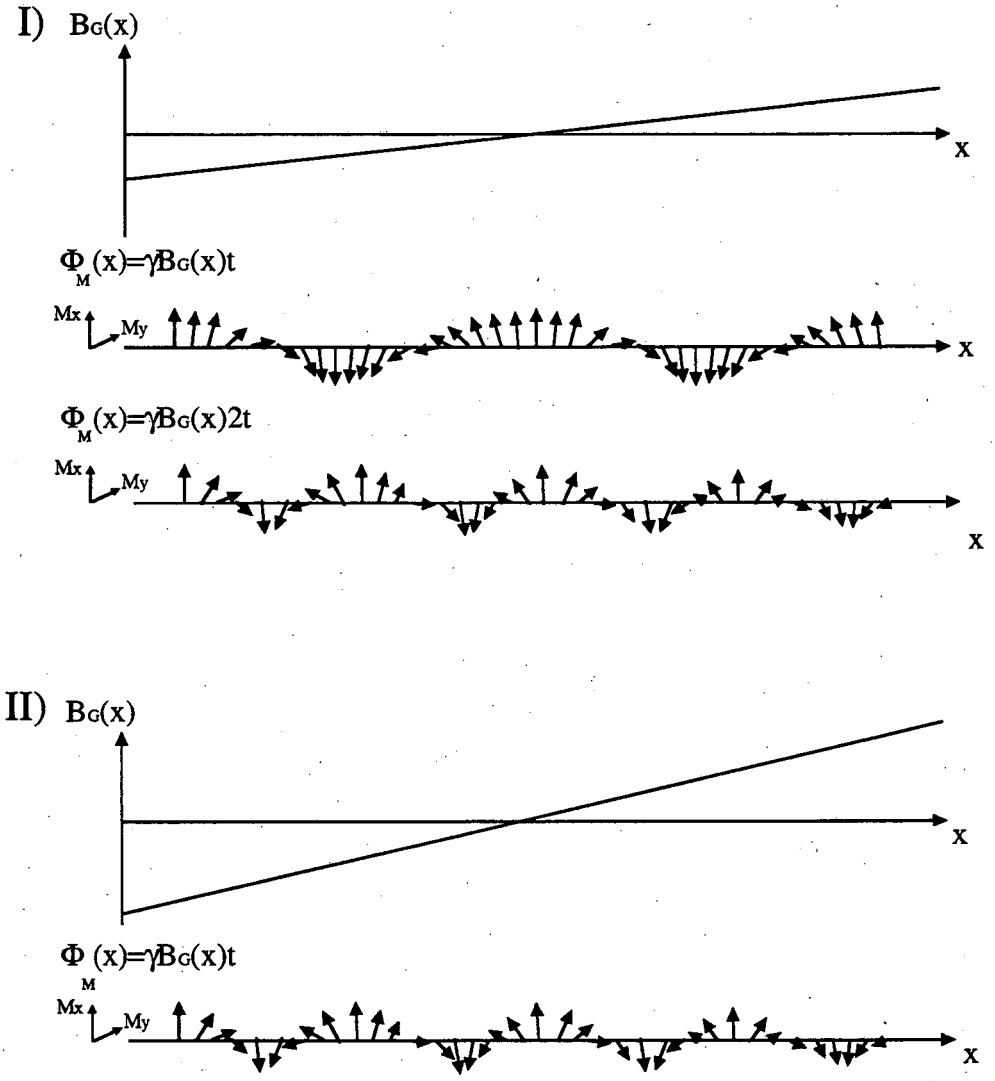

Figure 5.1: Helical phase distribution of spins resulting from magnetic field gradient. The gradient in I is half as large as the gradient in II. $B_G(x)$ is the gradient magnetic field strength. $\Phi_M(x)$ is the phase of the magnetization. t is the duration of the magnetic field gradient.

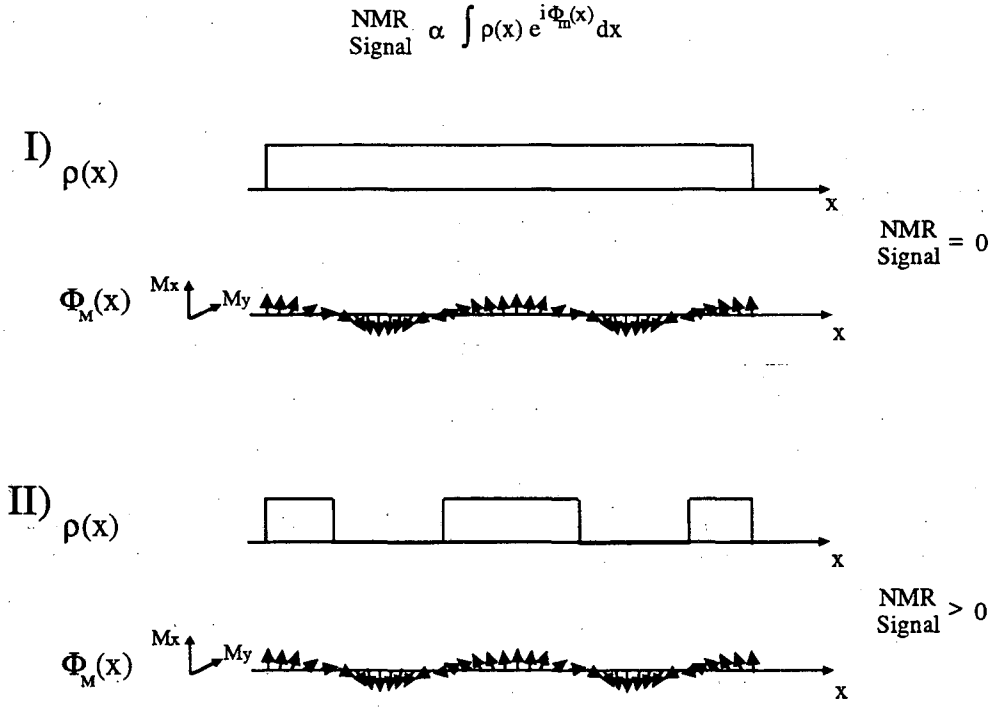

Figure 5.2: The helical phase distribution of the spins acts as a filter to detect spatial frequencies in the NMR phantom. $\rho(x)$ is the density of the nuclear spins. $\Phi_M(x)$ is the phase of the magnetization.

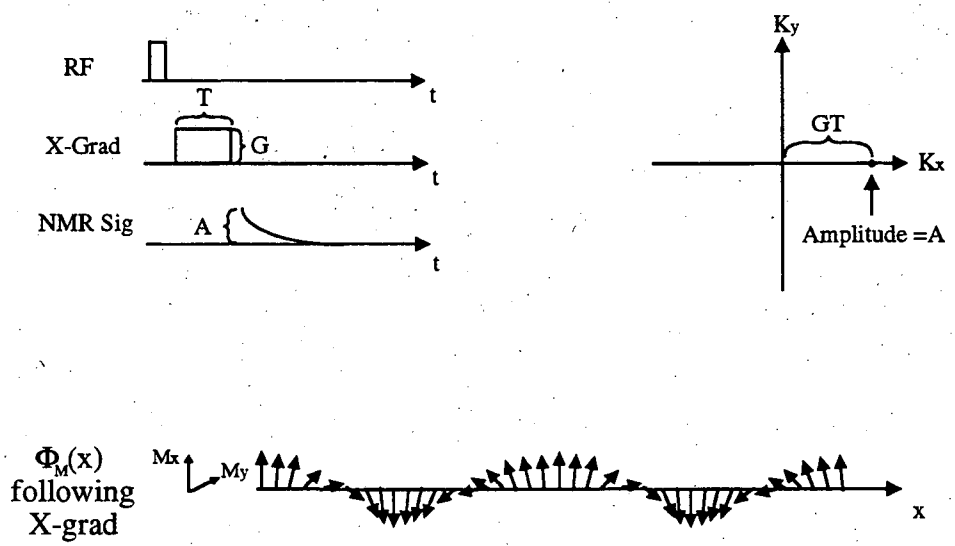

Figure 5.3: Phase encode sampling of NMR phantom's spatial frequencies. The sampled spatial frequencies are depicted with a k-space representation. A single spatial frequency is sampled for each phase encode gradient. A number of experiments each using a different phase encode gradient must be used in order to sample many points in k-space.

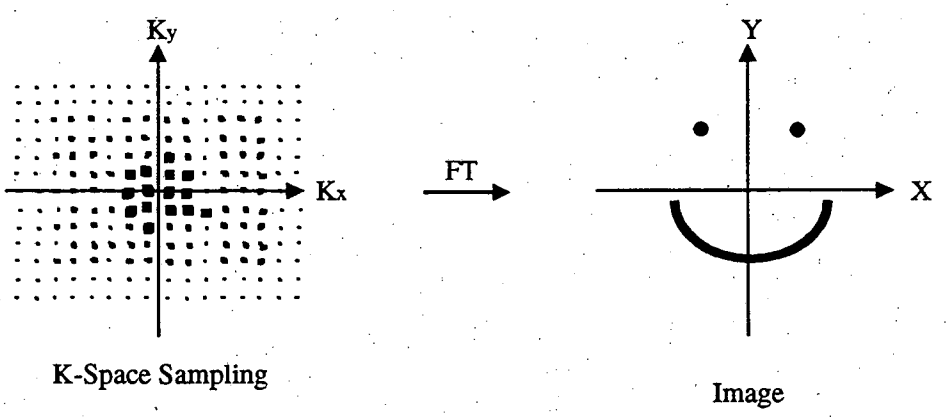

Figure 5.4: The Fourier Transform of the sampled k-space points produces an image of the NMR phantom.

frequency of the helical distribution of the spin phases first unwinds and then winds up again. A number of spatial frequencies are sampled so that a line in k-space is sampled. A drawback to using read-out gradients is that the NMR image field of view constrains the sampling period. Constraining the sampling period can lead to loss of SNR. Another drawback to using read-out gradients is that they are also sensitive to sample movement.

A third approach to encoding spatial information into a NMR signal is with

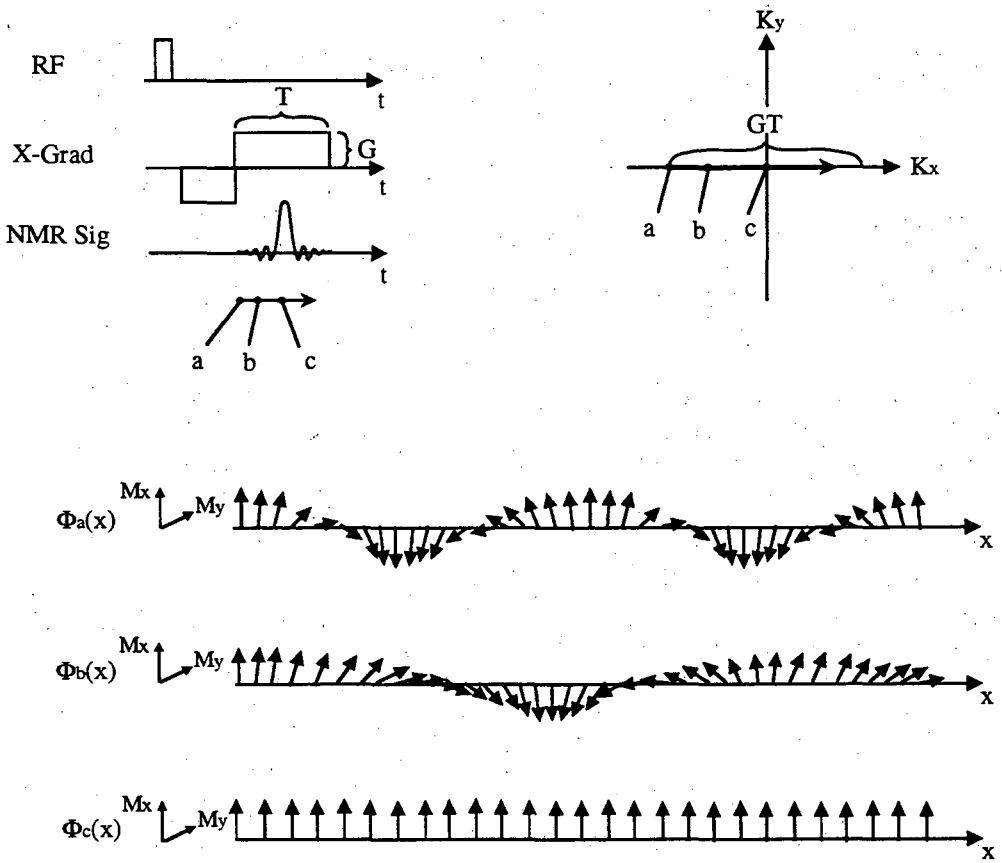

Figure 5.5: A Readout gradient sampling of the NMR phantom's spatial frequencies. A single experiment using a read-out gradient samples a line of k-space.

a echo-planar gradient [60], see Figure 5.6. A echo-planar gradient is similar to a read-out gradient, but instead of being constant it oscillates during the sampling. The effect of the oscillating gradient is to sample a whole plane of k-space from a single NMR FID.

Read-out gradients and echo-planar gradient approaches are useful for obtain-

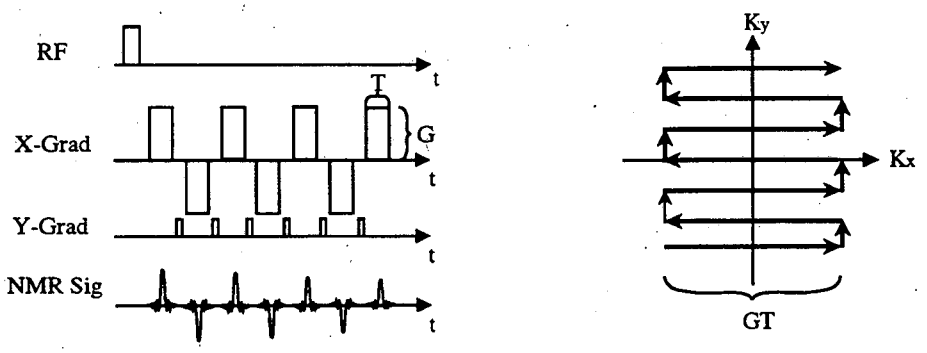

Figure 5.6: An echo-planar gradient sampling of the NMR phantom's spatial frequencies. A single experiment using a echo-planar gradient samples a whole plane of k-space.

ing complete sampling of k-space in short periods of time. Short k-space sampling times are helpful with regards to correcting for sample movement. If a sample moves between two complete samplings of k-space, a simple constant phase shift between the two complete k-space samplings will re-align them. One drawback of read-out and echo-planar techniques is that it is hard to get spectroscopic information from these images.

5.2 Principles of MQ Filtered Imaging

As discussed in Chapter 2, there are two types of multiple quantum filters: phase-cycled and gradient-selected. It is straightforward to use either technique for imaging by replacing the single excitatory RF pulse in the imaging sequence with the RF pulses of the MQ filter. Typically, the phase encode gradients are inserted during the sampling period of the MQ filter; however, it has been shown that these gradients can also be applied during the preparation or evolution periods [9, 10].

The advantage of using the PCMQ filter over the GSMQ filter is that it has a factor of two better SNR. As discussed in Chapter 2, GSMQ filter loses half of its

signal by only rephasing half of the spins with its refocusing gradient. The PCMQ filter does not have this problem since it does not ever dephase the spins.

A disadvantage of the PCMQ technique is that it requires excessively long imaging times. As mentioned previously the PCMQ filter requires up to 64 phase cycles. This means that k-space must be sampled completely 64 times. The multiple samplings of all of k-space required by PCMQ filtering is a serious problem since it is often very difficult to sample k-space once in a reasonable period of time. Another disadvantage is that the technique is very sensitive to flip angle variation resulting from RF inhomogeneity. The elimination of unwanted signals is achieved through subtraction. If the flip angle of the RF pulse varies due to RF inhomogeneity, then the subtraction is incomplete and spurious signals arise.

The advantages of the GSMQ technique are that it requires shorter imaging times, is insensitive to RF inhomogeneity, and is less sensitive to sample movement. A GSMQ filter is complete with only 4 RF pulses and no phase cycling so this technique requires only one complete sampling of k-space in contrast to the PCMQ filter. Since the elimination of the unwanted signals does not depend upon the RF flip angles, the GSMQ filter is insensitive to RF inhomogeneity. In principle, the GSMQ filters dephases all signals except the desired signals which are rephased by the refocusing gradient. The final advantage of the GSMQ filters is that they can be easily implemented with echo-planar imaging. Echo-planar images are easily corrected for sample movement. The disadvantage of the gradient-selected MQ filter is the factor of 2 lower SNR. One of the contributions of this thesis has been to show that this can be made up by using shorter repetition times, see Chapter 4.

5.3 PC2Q Filtered Imaging

5.3.1 Methods

As a part of studies directed towards developing MQ filtered ^{23}Na imaging at

fields above 2.35 Tesla, phase-cycled two-quantum filtered images of a ^{23}Na phantom were obtained with an Omega 4.7 Tesla NMR system (General Electric, Fremont, CA). A PC2Q filter was used in this study instead of a PC3Q filter since PC2Q filters require two-thirds as many phase-cycle steps as do PC3Q filters. The 4.7 T phantom consisted of two 2 cm diameters plastic balls, Phantom 1. One ball contained a 2.0 M aqueous NaCl solution and the other ball contained 2.0 M NaCl in a 4% agarose gel.

A three-dimensional one pulse image of Phantom 1 was taken using the sequence shown in Figure 5.7. The image parameters are shown in Table 5.1.

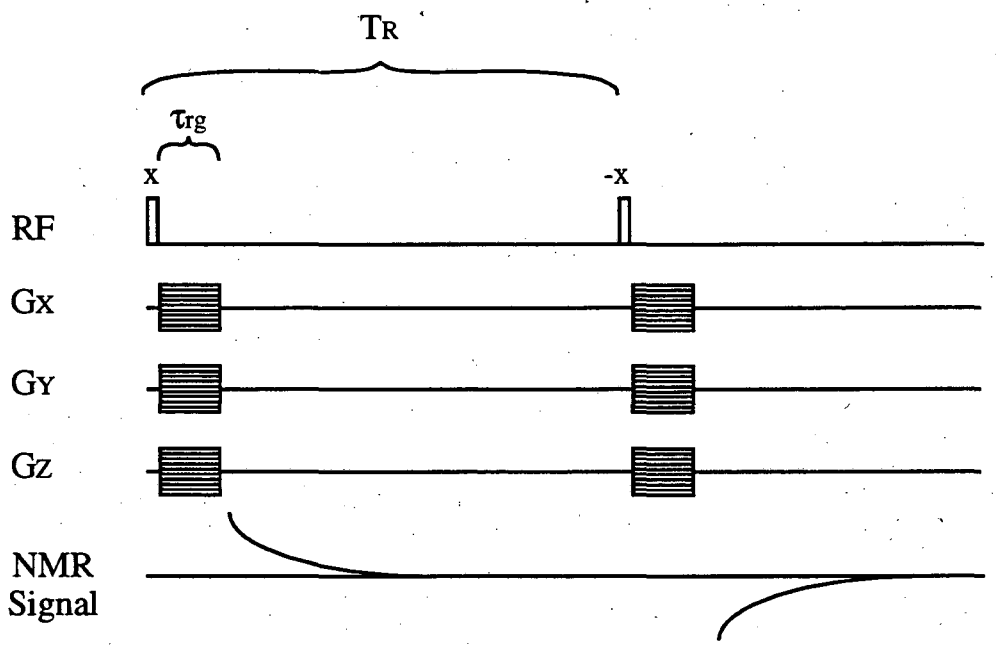

Figure 5.7: Pulse sequence used to obtain 1Q image in Figure 5.9. Sequence parameters are in Table 5.1.

TABLE 5.1

Three Dimensional One Pulse Image Parameters for Phantom 1

Parameter	Value
90° Pulse Duration	78 μs
Number of Points Sampled	512
Sampling Dwell	100 μs
τ_{rg}	0.5 ms
Number of Phase Encodes in Each Dimension	16
Field of View in Each Dimension	8 cm
Voxel Size	0.5 x 0.5 x 0.5 cm^3
T_R	150 ms
Imaging Time	20 minutes

A three dimensional PC2Q filtered image was obtained using three phase encoding gradients after the fourth RF pulse in the PC2Q filter. The pulse sequence for this imaging technique is shown in Figure 5.8. The experimental parameters for the PC2Q filtered image are listed in Table 5.2.

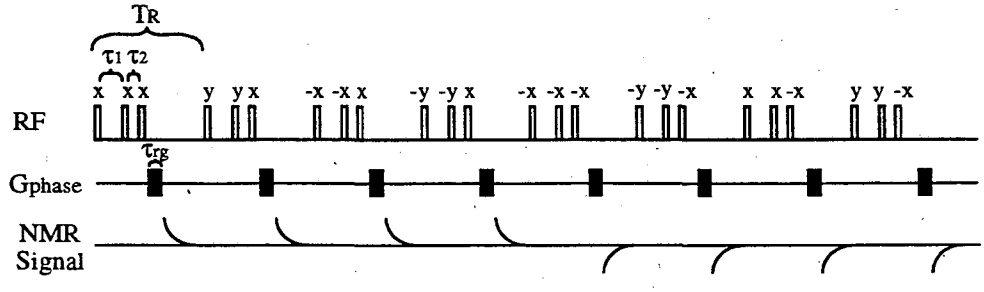

Figure 5.8: Pulse sequence used to obtain phase-cycled two-quantum filtered image in Figure 5.9. Sequence parameters are in Table 5.2.

TABLE 5.2
Three Dimensional Phase-Cycled Double-Quantum Filtered Image Parameters

Parameter	Value
90° Pulse Duration	78 μs
τ_1	5.0 ms
τ_2	10 μs
Number of Points Sampled	512
Sampling Dwell	100 μs
τ_{rg}	0.5 ms
Number of Phase Encodes in Each Dimension	16
Field of View in Each Dimension	8 cm
Voxel Size	0.5 x 0.5 x 0.5 cm^3
T_R	150 ms
Imaging Time	80 minutes

The suppression factor for the PC2Q imaging experiments was determined by dividing the signal amplitude of the aqueous ^{23}Na ball in the one pulse image by the amplitude of this signal in the PC2Q filtered image.

5.3.2 Results

The one pulse image of the Phantom 1 is shown in Figure 5.9. The PC2Q filtered image of the Phantom 1 is shown also in Figure 5.9. The imaging time for the PC2Q filtered image was four times that of the conventional one pulse image due to the four phase-cycling steps of the PC2Q filter. This four step PC2Q filter suppressed the ^{23}Na signal from the 2.0 M NaCl ball by a factor of 240. Improved suppression would require additional phase-cycling steps which would make the PC2Q imaging

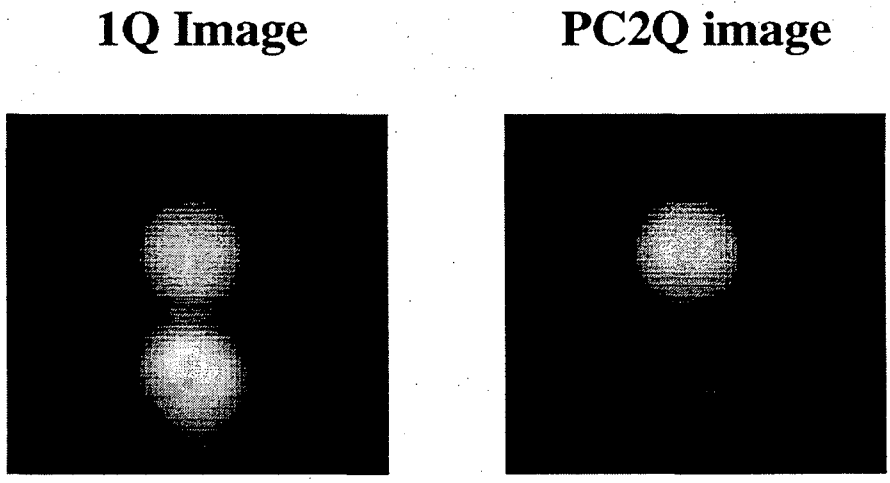

Figure 5.9: Slices from three dimensional ^{23}Na images acquired at 4.7 Tesla. The top 2 cm sphere contains 2.0 M NaCl in a 4% agarose gel. The bottom 2 cm sphere contains 2.0 M Aqueous NaCl. See Tables 5.1 and 5.2 for image parameters.

5.4 Modified GS3Q Filtered Imaging

5.4.1 Methods

For the modified GS3Q images a 8.5 cm x 7 cm plastic ellipsoid containing two 4 cm diameter plastic spheres was used (Phantom 2). The NaCl concentrations of Phantom 2 were chosen based on the concentrations and volume fractions of intracellular and extracellular ^{23}Na in the brain [1]. Phantom 2 contained a 0.03 M aqueous NaCl solution inside the ellipsoid and outside of the spheres, 0.012 M NaCl in a 4% agarose gel inside one sphere, and 0.024 M NaCl in a 4% agarose gel inside the other sphere.

A three-dimensional one pulse image of Phantom 2 was taken using the sequence

shown in Figure 5.10. The image parameters of the sequence are shown in Table 5.3. The one pulse image was obtained by zero-filling 32 x 32 x 32 points of data up to 64 x 64 x 64 points. The RF coil and 2.35 T magnet used are described in Section 4.2.

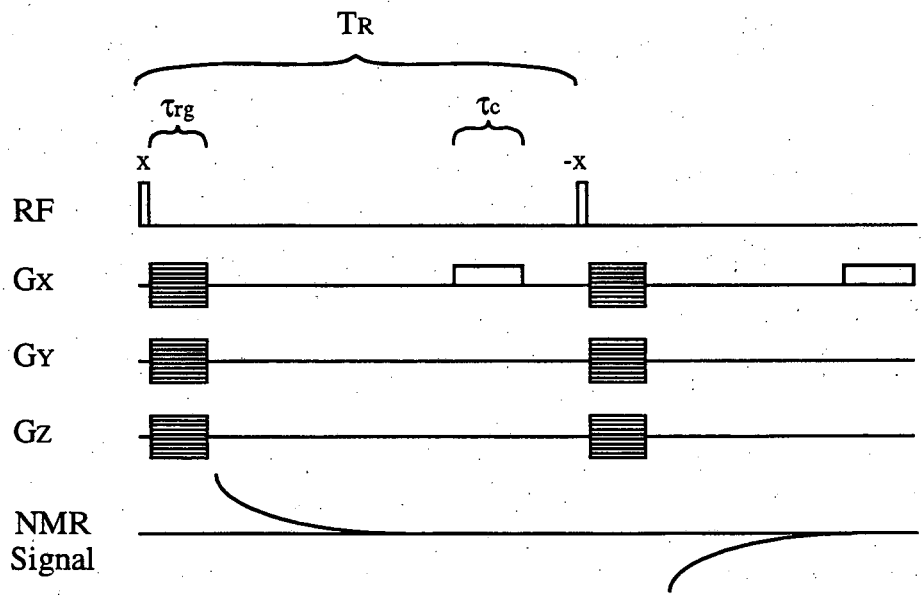

Figure 5.10: Pulse sequence used to obtain 1Q image in Figure 5.12. Sequence parameters are in Table 5.3.

TABLE 5.3

Three Dimensional One Pulse Image Parameters for Phantom 2

Parameter	Value
90° Pulse Duration	140 μs
Number of Points Sampled	256
Sampling Dwell	200 μs
τ_c	5.0 ms
Crusher Gradient Amplitude	0.3 G/cm
τ_{rg}	0.5 ms
Number of Phase Encodes in Each Dimension	32
Field of View in Each Dimension	24 cm
Voxel Size	0.75 x 0.75 x 0.75 cm^3
T_R	70 ms
Imaging Time	90 minutes

A three dimensional triple-quantum filtered image was obtained using three phase encoding gradients after the fourth and eighth RF pulses in the modified GS3Q filter. The pulse sequence for this imaging sequence is shown in Figure 5.11. The experimental parameters for the modified GS3Q filtered image are listed in Table 5.4. These experimental data were apodized with the function $D'_{11}(t,0)$.

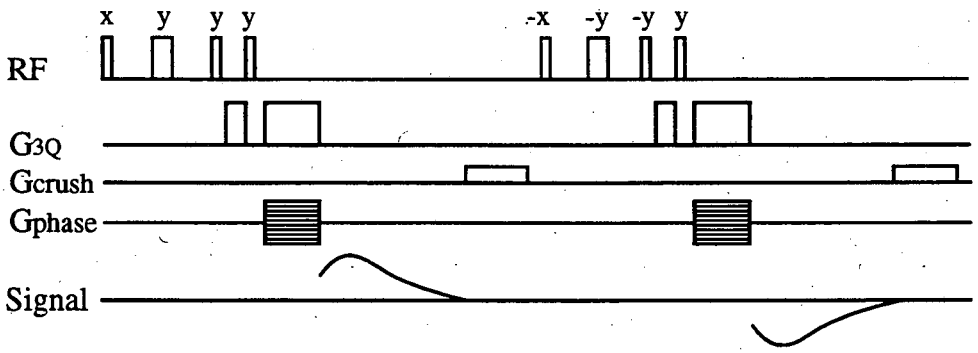

Figure 5.11: Pulse sequence used to obtain phase-cycled two-quantum filtered image in Figure 5.12. Sequence parameters are in Table 5.4 and Figure 2.9.

TABLE 5.4

Three Dimensional Gradient-Selected Triple-Quantum Filtered Image Parameters

Parameter	Value
Modified GS3Q Filter Parameters	Same as in Table 4.2
Number of Points Sampled	512
Sampling Dwell	100 μs
Number of Phase Encodes in Each Dimension	16
Field of View in Each Dimension	24 cm
Voxel Size	1.5 x 1.5 x 1.5 cm^3
T_R	70 ms
Imaging Time	54 minutes

Additional experiments were performed to determine the suppression factor in the GS3Q filtered image. In these experiments a third phantom was used. Phantom 3 consisted of a 8.5 cm x 7 cm plastic ellipsoid containing only a 0.3 M aqueous NaCl solution. The suppression factor for the imaging experiments was determined by dividing the signal strength of a modified GS3Q filtered image of Phantom 3 by the signal strength of a one pulse image of Phantom 3 which used the GS3Q image parameters listed in Table 5.4. These experimental data were apodized with the function $D'_{11}(t,0)$.

The spurious 1Q ^{23}Na signal from the 0.03 M aqueous NaCl solution in the modified GS3Q image of Phantom 2 was obscured by the measurement noise. The amplitude of this spurious 1Q ^{23}Na signal in this image was determined by two methods. In the first method the signal amplitude of a modified GS3Q filtered image of Phantom 3 was divided by 10. In the second method a one pulse image of Phantom 2 was taken using the GS3Q image parameters listed in Table 5.4. The maximum signal of this image, which was produced by 1Q signals from the 0.03 M aqueous NaCl, was multiplied by the suppression factor measured using Phantom 3. These experimental data were also apodized with the function $D'_{11}(t,0)$.

Experiments were performed to predict the SNR for a modified GS3Q filtered image of BER ^{23}Na in the human brain. SNR measurements from a 30 cm diameter, 30 cm long, 22 Mhz ^{1}H RF Alderman and Grant head coil loaded by a patient and SNR measurements from the 26 Mhz ^{23}Na RF birdcage coil loaded by Phantom 2 were compared. These measurements were made by determining the RF magnetic field produced per unit current for each coil and invoking reciprocity [61] and by measuring the noise for each coil.

5.4.2 Results

The one pulse image of Phantom 2 is shown in Figure 5.12. The modified GS3Q filtered image of Phantom 2 is shown also in Figure 5.12. The modified GS3Q filtered SNR of the 0.012 M and 0.024 M ^{23}Na, 4% agarose gel balls are 17 and 30. The suppression factor measured with Phantom 3 was 220 for the center 1.5 x 1.5 x 1.5 cm^3 voxel and 450 for all of the other 1.5 x 1.5 x 1.5 cm^3 voxels. The decreased suppression factor for the center voxel is attributed to inadequate dephasing of steady state transverse magnetization. Both of the methods discussed in the Imaging Methods section to determine the amplitude of the spurious 1Q signal from the 0.03 M aqueous NaCl in the modified GS3Q filtered image of Phantom 2 show the SNR of

the spurious 1Q signal to be 1.5.

The measurements to determine the SNR for a modified GS3Q filtered image of BER ^{23}Na in a human head human head show a factor of four reduction in SNR for the human head compared to the SNR obtained for the modified GS3Q filtered image in Figure 5.12. To maintain the SNR and acquisition time of Figure 5.12 for a modified GS3Q filtered image of a human head, the voxel size would need to increase from 1.5 x 1.5 x 1.5 cm^3 to 2.0 x 2.0 x 2.0 cm^3 and the RF head coil would need to be used in quadrature. Using the above results it can be predicted that for a 30 minute modified GS3Q filtered imaging time of a human head at 2.35 T, using a T_R of 70 ms, and with 2.0 x 2.0 x 2.0 cm^3 voxels a SNR of 10 should be obtained for 0.012 M ^{23}Na with relaxation times similar to those in Table 4.1.

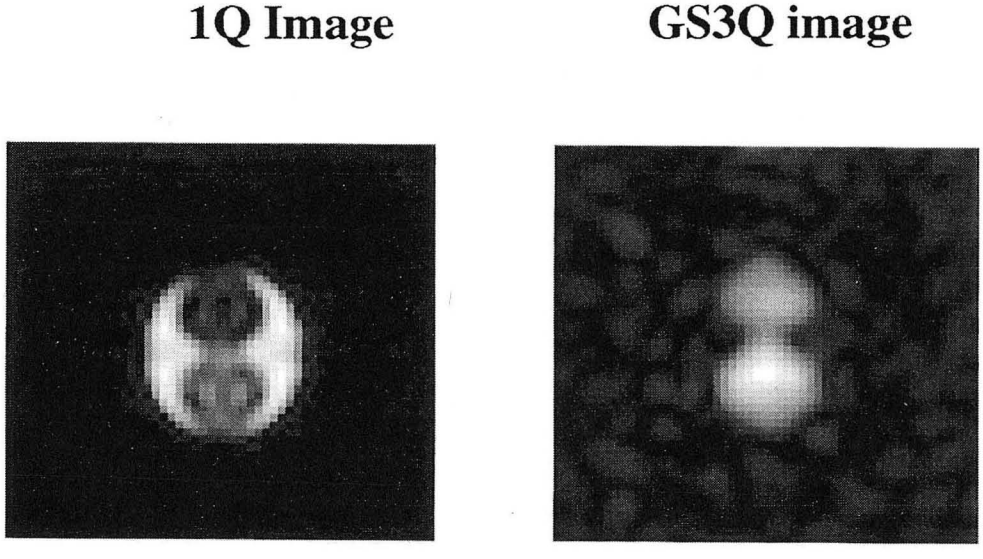

Figure 5.12: Slices from three dimensional ^{23}Na images acquired at 2.35 Tesla. The top 4 cm sphere contains 0.012 M NaCl in a 4% agarose gel. The bottom 4 cm sphere contains 0.024 M NaCl in a 4% agarose gel. The surrounding solution contains 0.030 M Aqueous NaCl. See Tables 5.3 and 5.4 for image parameters.

Chapter 6

Conclusion

In this chapter the contributions of this thesis are reviewed and a few directions for future research are discussed. The directions for future research include experiments using ^{23}Na nuclei and ^{1}H nuclei.

6.1 Contributions of Thesis

The first contribution of this thesis is demonstrating that significant signal to noise improvements can be obtained by using multiple-quantum filters with short repetition times. The second contribution was to show that the use of multiple-quantum filters with short repetition times is complicated by spurious one quantum signals arising from steady state dynamics. The third contribution of this thesis is to show that calculations with irreducible superoperators can be instrumental in designing new multiple-quantum filter sequences to suppress spurious one-quantum signals. The fourth contribution was to use the irreducible superoperators to develop the modified GS3Q filter. The fifth contribution was to measure all six relaxation times for ^{23}Na in an agarose gel using a 2.35 Tesla static magnetic field. The final, and I believe most significant, contribution was to obtain multiple-quantum filtered

images of ^{23}Na at physiological concentration using the modified GS3Q filter. This last contribution enabled me to predict that multiple-quantum filtered imaging of ^{23}Na in human brains should be possible.

6.2 Future Research

One direction for new research is to find new multiple-quantum filtered techniques with better suppression characteristics than the one described here. Techniques that can be used to improve the suppression are additional phase cycling and incrementing the phase of the RF pulses. The utilization of additional phase cycles is limited only by the length of the experiment. In a 30 minute experiment it should be possible to use up to 8 phase-cycle steps in a 16 x 16 x 16 voxel image. There are up to 64 phase-cycle steps used in a complete PCMQ filter. It remains to be determined which combination of 8 of the 64 phase-cycle steps is best for suppressing spurious steady state signals from GS3Q filters. A very interesting approach to suppressing steady state artifacts from one pulse experiments by incrementing the RF phase has been developed [62]. Applying this approach to minimizing the spurious steady state signals of multiple-quantum filters could be very fruitful.

Additional avenues of research involve understanding ^{23}Na multiple-quantum signals in humans. It remains to be resolved if MQ ^{23}Na signals are produced disproportionately by intracellular ^{23}Na. If this is the case, then ^{23}Na MQ signals will be markers for intracellular ^{23}Na. If this is not the case, then ^{23}Na MQ signals will be valuable in obtaining images of restricted ^{23}Na versus hydrated ^{23}Na. Although it has been proposed that ^{23}Na MQ imaging may reveal valuable information regarding the pathophysiology of mental illness, cancer and ischemia, the utility of MQ filtered ^{23}Na imaging in humans largely remains undetermined.

Multiple-quantum filtering may prove extremely valuable in obtaining information from proton spectra. Proton spectra are complicated by many overlapping spectral lines. Multiple-quantum filtering can be valuable in eliminating some lines or can

be used with two-dimensional spectroscopy to resolve overlapping lines which survive the MQ filter. As with ^{23}Na, the signal to noise of *in vivo* proton spectra is rather low. To obtain as much signal to noise as possible in MQ filtered spectra it is essential to run the MQ filters with short repetition times. Substantial analysis remains to be performed in order to optimize short repetition time MQ filters for proton spectroscopic imaging.

Bibliography

[1] S.K. Hilal, A.A. Maudsley, J.B. Ra, H.E. Simon, P. Roschmann, S. Wittekoek, Z.H. Cho, and S.K. Mun. In vivo NMR imaging of sodium-23 in the human head. *Journal of Computer Assisted Tomography*, 9:1–7, 1985.

[2] R. H. Grifffey, B. Griffey, K. Berghmans, C. Gasparovic R. Wenk, and P. Mann. Sodium multiple quantum spectroscopy and imaging of tumor cells implanted in nude rats and in cell suspensions. *Book of Abstr., Soc. Magn. Reson. Med. 7^{th} Ann. Meeting*, 1:213, 1988.

[3] R.C. Lyon, J. Pekar, C.T.W. Moonen, and A.C. McLaughlin. Double-quantum surface-coil NMR studies of sodium and potassium in the rat brain. *Magn. Reson. Med.*, 18:80–92, 1991.

[4] H.J.C. Berendsen and H.T. Edzes. The observation and general interpretation of sodium magnetic resonance in biological material. *Ann. N.Y. Acad. Sci.*, 204:459–485, 1973.

[5] J. Pekar and J.S. Leigh. Detection of biexponential relaxation in sodium-23 facilitated by double-quantum filtering. *J. Magn. Reson.*, 69:582, 1986.

[6] J. Pekar, C.T.W. Moonen, and D.I. Hoult. Three-quantum imaging of sodium-23. *Book of Abstr., Soc. Magn. Reson. Med. 8^{th} Ann. Meeting*, page 670, 1989.

[7] R.H. Griffey, B.V. Griffey, and N.A. Matwiyoff. Triple-quantum-coherence-filtered imaging of sodium ions *in vivo* at 4.7 Tesla. *Magn. Reson. Med.*, 13:305, 1990.

[8] M.D. Cockman, L.W. Jelinski, J. Katz, D.D. Sorce, L.M. Boxt, and P.J. Cannon. Double-quantum-filtered sodium imaging. *J. Magn. Reson.*, 90:9–18, 1990.

[9] S. Wimperis and B. Wood. Triple-quantum sodium imaging. *J. Magn. Reson.*, 95:428, 1991.

[10] S. Wimperis, P. Cole, and P. Styles. Triple-quantum filtration NMR imaging of 200 mM sodium at 1.9 Tesla. *J. Magn. Reson.*, Private Communication, 1991.

[11] P.S. Aronson. Kinetic properties of the plasma membrane $^{23}Na^{+}-^{1}H^{+}$ exchanger. *Ann. Rev. Physiol.*, 47:545–560, 1985.

[12] J.W. Deitmer and W.R. Schlue. An inwardly directed electrogenic sodium-bicarbonate co-transprot in leech glial cells. *J. Physiol.*, 411:179–194, 1989.

[13] R.C. Thomas. Experimental displacement of intracellular pH and the mechanism of its subsequent recovery. *J. Physiol.*, 354:3P–22P, 1984.

[14] S.K. Hilal, J.B. Ra, C.H. Oh, I.K. Mun, S.G. Steven, and P. Roschmann. *Magnetic Resonance Imaging (Ch. 31)*. Mosby, 1988.

[15] F.K. Goodwin and K.R. Jamison. *Manic-Depressive Illness.* Oxford Univ. Press, 1990.

[16] J. Andrasko. Nonexponential relaxation of ^{23}Na in agarose gels. *J. Magn. Reson.*, 16:502, 1974.

[17] G.S. Payne and P. Styles. Multiple-quantum-filtered ^{23}Na NMR spectroscopy in model systems. *J. Magn. Reson.*, 95:253–266, 1991.

[18] L.A. Jelicks and R.K. Gupta. Observation of intracellular sodium ions by double-quantum filtered ^{23}Na NMR with paramagnetic quenching of extracellular coherence by gadolinium tripolyphosphate. *J. Magn. Reson.*, 83:146–151, 1989.

[19] B.D. Foy and D.B. Burstein. Characteristics of extracellular sodium relaxation in perfused hearts with pathologic interventions. *Private Communication*, 1992.

[20] J.H. Lee, Y. Seo, M. Murakami, C. Labadie, and S. Springer. SR-free discrimination of compartmental ^{23}Na resonances by relaxographic analysis. *Book of Abstr., Soc. Magn. Reson. Med.* 11^{th} *Ann. Meeting*, works in progress:2222, 1992.

[21] J. Pekar, L. Ligeti, Z. Ruttner, T. Sinnwell, C.T.W. Moonen, and A.C. McLaughlin. Combined ^{31}P triple quantum filtered ^{31}Na NMR studies of ischemia in the cat brain. *Book of Abstr., Soc. Magn. Reson. Med.* 10^{th} *Ann. Meeting*, 1:149, 1991.

[22] Christopher Sotak. *Private Communication*, 1993.

[23] W.D. Rooney and C.S. Springer. A comprehensive approach to the analysis and interpretation of the resonances of spins 3/2 from living systems. *NMR Biomed.*, 4:209–226, 1991.

[24] W.D. Rooney and C.S. Springer. The molecular environment of intracellular sodium: ^{23}Na NMR relaxation. *NMR Biomed.*, 4:227–245, 1991.

[25] C. Labadie, T.M. Button, W.D. Rooney, J.H.L. Lee, and C.S. Springer. Relaxographic imaging. *Book of Abstr., Soc. Magn. Reson. Med.* 10^{th} *Ann. Meeting*, works in progress:1218, 1991.

[26] J.H. Lee, C. Labadie, and S. Springer. Relaxographic analysis of ^{23}Na resonances. *Book of Abstr., Soc. Magn. Reson. Med.* 11^{th} *Ann. Meeting*, 2:2214, 1992.

[27] A. Bax, R. Freeman, and S.P. Kempsell. Natrual abundance ^{13}C-^{13}C coupling observed via double-quantum coherence. *J. Amer. Chem. Soc.*, 102:4849–4851, 1980.

[28] R. R. Ernst and W. A. Anderson. Application of fourier transform spectroscopy to magnetic resonance. *Rev. Sci. Instrum.*, 37:93–102, 1966.

[29] C.P. Slichter. *Principles of Magnetic Resonance.* Springer-Verlag, 1990.

[30] R.R. Ernst, G. Bodenhausen, and A. Wokaun. *Principles of Nuclear Magnetic Resonance in One and Two Dimensions.* Clarendon Press, 1987.

[31] G. Bodenhausen. Multiple-quantum NMR. *Progress in NMR Spectroscopy*, 14:137–173, 1981.

[32] O.W. Sorensen, G.W. Eich, M.H. Levitt, G. Bodenhausen, and R.R. Ernst. Product operator formalism for the description of NMR experiments. *Progress in NMR Spectroscopy*, 16:163–192, 1983.

[33] M. Munowitz and A. Pines. Principles and applications of multiple-quantum NMR. *Advances in Chemical Physics*, 66:1–152, 1987.

[34] A. Abragam. *Principles of Nuclear Magnetism.* Oxford, 1985.

[35] I.I. Rabi, J.R. Zacharias, S. Millman, and P. Kusch. A new method of measureing nuclear magnetic moment. *Phys. Rev.*, 53:318, 1938.

[36] F. Bloch, W.W. Hansen, and M. Packard. The nuclear induction experiment. *Phys. Rev.*, 70:474, 1946.

[37] D. Newitt. *Nuclear Quadrupole Induced Electric Polarization in GaAs.* Ph.D. Thesis Dissertation - U.C. Berkeley, 1993.

[38] G.J. Bowden, W.D. Hutchinson, and J. Khachan. Tensor operator formalism for multiple-quantum NMR. 2. Spins 3/2, 2 and 5/2 and general I. *J. Magn. Reson.*, 67:415–437, 1986.

[39] A.L. Van Geet. Hydration number of sodium ions determined by sodium magnetic resonance. *J. Amer. Chem. Soc.*, 94:5583–5587, 1972.

[40] T.E. Bull. Nuclear magnetic relaxation of spin-3/2 nuclei involved in chemical exchange. *J. Magn. Reson.*, 8:344–353, 1972.

[41] M.J. Kushmerick and R.J. Podolsky. Ionic mobility in muscle cells. *Science*, 166:1297–1298, 1969.

[42] P. Laszlo. Sodium-23 nuclear magnetic resonance spectroscopy. *Angew. Chem. Int. Ed. Engl.*, 17:254–266, 1978.

[43] A.G. Redfield. On the theory of relaxation processes. *IBM J. Res. Dev.*, 1:19, 1957.

[44] G. Jaccard, W. Wimperis, and G. Bodenhausen. Multiple-quantum NMR spectroscopy of S=3/2 spins in isotropic phase: A new probe for multiexponential relaxation. *J. Chem. Phys.*, 85:6282, 1986.

[45] P.S. Hubbard. Nonexponential nuclear magnetic relaxation by quadrupole interactions. *J. Chem. Phys.*, 53:985–987, 1970.

[46] M. Eisenstadt and H.L. Friedman. Nuclear magnetic relaxation in ionic soluion. I. Relaxation of ^{23}Na in aqueous solutions of NaCl and $NaClO_4$. *J. Chem. Phys.*, 44:1407–1414, 1965.

[47] H.G. Hertz. Magnetic relaxation by quadrupole interactions of ionic nuclei in electrolyte solutions part I: Limiting values for infinite dilution. *Benchte der Bansen-Gesellschaft*, pages 531–540, 1973.

[48] A. Wokaun and R.R. Ernst. Selective detection of multiple quantum transitions in NMR by two-dimensional spectroscopy. *Chem. Phys. Lett.*, 52:407–412, 1977.

[49] J. Jeener. Ampere International Summer School. Yugoslavia. 1971.

[50] W.P. Aue, E. Bartholdi, and R.R. Ernst. Two-dimensional spectroscopy. Application to nuclear magnetic resonance. *J. Chem. Phys.*, 64:2229–2246, 1976.

[51] A. Bax, P.G. DeJong, and J. Smidt. Separation of the different orders of NMR multiple-quantum transitions by the use of pulsed field gradients. *Chem. Phys. Lett.*, 69:567–570, 1980.

[52] R. Kaiser, E. Bartholdi, and R.R. Ernst. Diffusion and field-gradient effects in NMR Fourier spectroscopy. *J. Chem. Phys.*, 60:2966, 1974.

[53] C.T.W. Moonen and P.C.M. Van Zigal. Highly effective water suppression for in vivo proton NMR spectroscopy (drysteam). *J. Magn. Reson.*, 88:28, 1990.

[54] M.E. Rose. *Elementary Theory of Angular Momentum.* John Wiley and Sons, 1957.

[55] N. Muller, G. Bodenhausen, and R.R. Ernst. Relaxation-induced violations of coherence transfer-selection rules in nuclear magnetic resonance. *J. Magn. Reson.*, 75:297, 1987.

[56] D.A. Varshalovich, A.N. Moskalev, and V.K. Khersonskii. *Quantum Theory of Angular Momentum.* World Scientific, 1988.

[57] A.D. McLachlan. Line widths of electron resonance spectra in solution. *Proc. R. Soc. London*, A280:271–288, 1964.

[58] W.S. Hinshaw and A.H. Lent. An introduction to NMR imaging: From Bloch equation to the imaging equation. *Proceedings of the IEEE*, 71(3):338–350, 1983.

[59] D.B. Twieg. The k-trajectory formulation of the NMR imaging process with applications in analysis and synthesis of imaging methods. *Med. Phys.*, 10:610–621, 1983.

[60] P. Mansfield and P.G. Morris. *NMR Imaging in Biomedicine.* Advances in Magnetic Resonance, Suppl. 2, 1982.

[61] D.I. Hoult and R.E. Richards. The signal-to-noise ratio of the nuclear magnetic resonance experiment. *J. Magn. Reson.*, 24:71, 1976.

[62] Y. Zur, S. Stokar, and P. Bendel. An analysis of fast imaging sequences with steady-state transverse magnetization refocusing. *Magn. Reson. Med.*, 6:175–193, 1988.

LAWRENCE BERKELEY LABORATORY
UNIVERSITY OF CALIFORNIA
TECHNICAL INFORMATION DEPARTMENT
BERKELEY, CALIFORNIA 94720